行政院原子能委員會

委託研究計畫研究報告

【太陽能及乙醇／氫氣轉換之量子化學計算模擬及實驗驗證】

【Quantum Simulations of Solar Energy and Ethanol to Hydrogen Conversion Processes with Experimental Validations】

計畫編號：962001 INER 0028

受委託機關(構)：國立交通大學

計畫主持人：林明璋

核研所參與人員：謝宏明

聯絡電話：(03)5731696

E-mail address：chemmcl@emory.edu

報告日期：96 年 11 月 23 日

目　錄

中文摘要

本計畫是為期四年行政院原子能委員會委託研究計畫之第三年執行結果摘要。這一年主要的工作在繼續進行以下兩個目標：1. 利用大型電腦計算解釋 InN/TiO_2 太陽能電池的製作機制及 InN 與 TiO_2 之間利用量子點及有效的化學鍵製作方法。2. 理論與實驗驗證 L. D. Schmidt 的 Rh/CeO_2 乙醇轉換氫氣催化劑的性能，並進而研究發現新而便宜的催化劑。

在乙醇轉換氫的實驗上，今年實驗結果發現，Ru/CeO_2/Al_2O_3 催化分解乙醇與水的混合物目前已得到 120%的轉換率，Ru 金屬比 Rh 較便宜 25 倍；另外，研究 CeO_2 與 ZrO_2 混合氧化物的實驗已在進行中。

大型量子計算可分為三方面，1. 乙醇轉氫在不同催化劑表面反應基制的研究。2. 量子點在 TiO_2 表面吸附的能量與結構。3. 發展 SCC-DFTB 將應用於乙醇轉氫及量子點/TiO_2 方面大型計算的元素參數。

在乙醇轉氫方面的計算，今年主要在了解水氣轉氫 ($CO+H_2O \rightarrow CO_2+H_2$) 在 Rh/$CeO_2$ 上的反應機制及能量。也進行乙醇在 Rh/CeO_2/ZrO_2 催化劑上的吸附及分解，同時，CuO/Al_2O_3 對乙醇轉氫的可行性也在計算中。

在量子點/TiO_2 系統的計算，今年著重於$(InN)_x$/OY(O)O/TiO_2 (Y=B and P)及$(Si)_x$ 量子點兩系統的研究，不同量子點的大小影響 TiO_2 帶隙的計算，已供給良好的結果。

在 SCC-DFTB 程式的發展，目前也有很好的進展，這個程式的完成，將可供給本計算團隊用 VASP 及 CASTEP 以外作大型分子群

的計算，諸如 $Ru_x/CeO_2/Al_2O_3$ 催化系統應用於乙醇轉氫的反應機制，將可用此程式研究並得反應速度常數。

除了上述的計算外，H_2S、H_2O_2 及 H_3BO_3 在 TiO_2 表面反應的計算已完成；類似計算研究以 H_3PO_3 作 InN 及 TiO_2 中間的 linker 已在進行中，此系列的反應，與 InN、InO_x 及 InS_x 的沉積亦有直接關係。

Abstract

This is the report for the third of the 4-year research project on the computational and experimental studies of the InN/TiO_2 system and/or the catalytic conversion of ethanol to hydrogen by the Schmidt type technique employing the Rh/CeO_2 and other catalysts. Our goals are two-fold: 1. Utilization of the large scale computation to elucidate processes relevant to the InN/TiO_2 solar cell system including quantum-dot and chemical functional-group modifications of the $InN\text{-}TiO_2$ interface; 2. Experimental and computational studies of Schmidt's ethanol to H_2 conversion processes in order to search for cheaper and equally efficient catalysts.

For the ethanol to H_2 conversion studies, experimentally we have demonstrated that the $Ru/CeO_2/Al_2O_3$ catalyst performed better than Schmidt's $Rh/CeO_2/Al_2O_3$ catalyst, reaching >120% H_2 conversion efficiency from autothermal oxidation with mixtures of C_2H_5OH and H_2O. Ru is cheaper than Rh commercially by a factor of 25.

Computationally, we have continually focused on three aspects: 1. Catalytic conversion of ethanol to H_2; 2. Electronic structures of quantum dots (QDs) attached to TiO_2 nanoparticles; 3. Development of the SCC-DFTB (self-consistent charge-density functional theory tight-binding) method for large atomic/molecular cluster calculations.

For the ethanol to hydrogen conversion related calculations, we have completed the study of the H_2O+CO water-gas shift reaction on the Rh/CeO_2 catalyst. The reaction was found to be obeying the Langmuir-Hinshelwood mechanism through chemisorption of both H_2O and CO on Rh (for CO) and/or Ce (for H_2O) sites, followed by the

dissociation of H_2O(a) and oxidation of CO(a) by HO(a). In addition, calculations for adsorption and decomposition of ethanol on Rh/CeO_2-ZrO_2 and CuO/Al_2O_3 have also been finished.

For the QD/TiO_2 related calculations, focus has been placed on $(InN)_n/OY(O)O/TiO_2$ (n=1-10) (Y=B and P) and $(Si)_x$ (x>100). The effects of QD-sizes on the system's band gap have been clearly elucidated. Most importantly the effect of the OY(O)O linker between InN and TiO_2 has been interpreted.

For the development of the SCC-DFTB method, a basic code for the establishment of elemental parameters has been completed, and the effort on the conversion of binding properties of key elements involved in the fabrication of the QD-solar cells and ethanol to H_2 conversion is being made.

Aside from the aforementioned large practical systems, we have also carried out detailed potential energy surfaces for reactions of H_2S, H_2O_2 and H_3YO_3 (Y=B and P) on TiO_2 surfaces. These reactions are directly relevant to the OMCVD of the $(InN)_x/OY(O)O/TiO_2$ and $(InN)_x/QD/TiO_2$ systems, where the QD may be InO_x and InS_x.

壹、計畫緣起與目的

有鑑於地球能源問題已開始受到重視，尋求相關取代能源已是迫不及待，而目前以燃料電池及太陽能電池為首要研究目標。在燃料電池方便，由於考慮到環保上相關的問題，因此希望發展出一套良好的乙醇轉換為氫氣的系統。希望此套系統能得到最高的轉換效率，並且不對環境造成破壞影響。目前此方向之研究又以 Schmidt 所得到的將近百分之一百的轉換為最優[1]，而此相關研究中，最理想的狀況下，甚至可以得到百分之一百六十六的轉換效率，所以本次計劃將以此理論為根本，希望發產出更進一步的結果。

乙醇是一種"綠色"(環保)燃料，在台灣它可以利用糖或甘蔗等農產品發酵而製造。台灣的亞熱帶地理位置適合發展以乙醇作為未來可能的永續能源，尤其是在燃料電池的應用方面。很不幸的，乙醇目前無法直接地被用於燃料電池，因為它和碳氫化合物具有相同的碳原子位置的問題。燃燒電池除產生電能外，其副產物僅為水及熱能，因此具有低污染的優點，是一種可產生環保能源的方法。Schmidt 等人[1]所採用的一個策略就是利用貴重金屬，如: Pt 或 Rh 吸附在金屬氧化物，如: CeO_2 或 La_2O_3 上面。他們利用在陶瓷泡狀結構上的 Rh/CeO_2 觸媒可以達到 95% 以上之轉化率。他們利用乙醇和水的混合物，藉由眾所周知的水煤氧反應 $CO + H_2O \rightarrow CO_2 + H_2$ 之助，可以達到 115%的轉化率。這些令人振奮的結果顯示利用乙醇這種真正環保且不多產生 CO_2 的燃料來取代日漸昂貴且對環境極具殺傷力的石化燃料，如石油和天然氣，已經變為可能。

在太陽能電池的研究方面，最近，主持人與其研究群藉由有

機金屬化學沉積的方式 TiO_2 的奈米粒子上成長出不同厚度且品質優良的 InN 薄膜[2]，吸收光譜顯示吸收波段為 UV/visible 範圍內 390 nm 到 800 nm 波長的寬廣吸收。為了了解 InN 光敏化 TiO_2 奈米粒子薄膜的結構與電子能態及對吸收波長的影響以及促進電子由 InN 移轉到 TiO_2 奈米薄膜的效率，量子點及有效的化學鍵，諸如 Si 及 InP 量子點和-OB(O)O、-OP(O)OO、>Si(O)O 等化學根在 TiO_2 表面吸附能量必須估計。這類資料必須利用新進的量子計算軟體與高速電腦的工率才能得知，故與國網中心的合作是非常必要的，因為台灣在這方面的大型計算尚遠落後於日本、美國及歐盟國家。

以超級電腦進行大尺度的計算以模擬相關化學反應及物理現象已經變成尖端材料研究及元件製造的一個不可或缺的部份。此種模擬計算可以幫助吾人瞭解所欲研究的系統中支配的物理法則及化學機制，因而提昇研究品質及產品開發的效率。在這方面，台灣是遠落於美國、日本和歐洲之後。為了增進台灣利用大型計算的能力，尤其是改進 InN/TiO_2 奈米粒子太陽電池之製程及效率[2]以及乙醇-氫氣的催化轉化效率[1]，我們擬模擬 InN 薄膜沉積的反應，尤其是將重點放在利用自組官能基形成奈米量子點的過程，並研究其與不同頻帶邊(band edge)之金屬氧化物混合之效應。我們也將研究乙醇催化轉化成氫氣的機制，希望能夠找到一個比最近 Schmidt 等人[1]所提出來的 Rh/CeO_2 更為價廉且更具效率的非均相觸媒。

此計劃將專注於利用最先進的量子化學計算，系統化地研究在含有 Si, InP 及其他金屬氧化物量子點的 $InN/QDs/TiO_2$ 系統中，使 TiO_2 奈米粒子表面官能化的反應機構以及乙醇在吸附在 CeO_2, La_2O_3, Al_2O_3 等金屬氧化物基質的貴重金屬 (如: Rh, Ru, Pt, etc.)的轉化機

制，並比較不同金屬的催化效率，以瞭解其催化的基本物理及化學原理。一旦催化劑的催化明確性以及其金屬氧化物基質的關連作用被瞭解，則我們可以利用量子化學理論計算探尋較具經濟效益的金屬催化物及其金屬氧化物基質；吸附在 Al_2O_3, TiO_2 或 ZnO 等奈米粒子上面的 Fe, Co, Cu 或 Ag 金屬奈米粒子的催化作用將會被仔細地研究。為了落實理論計算的結果，我們亦將利用一個類似 Schmidt 等人[1]所使用的小型的反應系統，以實驗來測量理論計算所建議的觸媒及其金屬氧化物基質的乙醇轉化效率。理論與實驗相結合來研究 InN/TiO_2 沉積以及乙醇-氫氣轉化過程，將可對其將來在工業上的應用提供寶貴的資訊。

References:

1. G. A. Deluga, J. R. Salge, L. D. Schmidt, X. E. Verykios, Science, 2004, 303, 993.
2. Jeng-Han Wang and M. C. Lin, ChemPhysChem, 2004, 5, 1615

貳、研究方法與過程

一、Ethanol to H_2 conversion:

(一) J. J. Ho（何嘉仁）：

We applied the periodic density-functional theory (DFT) to investigate the dehydrogenation of ethanol and the followed steam reforming reactions on the $4Rh/CeO_2$ (111) surface. We assumed that one O_2 molecule diffused into the O vacancy on $4Rh/CeO_{2-X}$ (111) surface, and under this circumstance, the adsorption energy of ethanol adsorbed on the surface was calculated to be -16.1 kcal/mol. Before forming a five-membered ring of an oxametallacyclic compound, the hydrogen atom of O-H and that of one β-carbon hydrogen from ethanol are first eliminated. The dehydrogenation reaction continues with the loss of two hydrogens from the α-carbon, at the same time, transforming to four-membered ring species ($Rh\text{-}CH_2CO\text{-}Rh$). Scission of the C-C bond occurs at this stage with a dissociation barrier 17.6 kcal/mol. Finally, the adsorbed products of CO、CH_2 and 4H could be observed. In the steam reforming process ($CH_2 + H_2O$), the hydrogen dissociation of CH_2 and H_2O occurs first, forming the species CH and OH, respectively. The CH prefers to associate with OH to form intermediate CHOH rather than further dissociates into C and H. The intermediate CHOH then dissociates the two hydrogens consecutively and forms CO and 2H. Finally, the adsorbed products of CO and 4H could be observed.

On the basis of the oxygen storage capacity (OSC) of ceria (CeO_2) and the dissociation of C-C bond activated by Rhodium, the

Rh/CeO_2 is considered to be a suitable catalyst for decomposition of ethanol. We apply the density-functional theory (DFT) to calculate the possible pathways for the dehydrogenation of ethanol and steam reforming reactions (CH_2 + H_2O) on a $4Rh/CeO_2$-(111)-(3x2) surface. Both the adsorbed intermediates and the reaction barriers in the dissociation pathways as well as the possible potential-energy surfaces are presented.

We applied plane-wave periodic density-functional theoretical calculation implemented in the Vienna ab initio simulation program (VASP). The generalized gradient approximation (GGA) of Perdew and Wang (PW91) was used for the exchange-correlation functional. The projector–augmented wave method (PAW), an all–electron method combining the accuracy of augmented plane waves with the cost–effective pseudopotentials implemented in VASP, is applied. The k-points set we used was 4x6x1with a spin polarized calculation. The Rh/CeO_2(111) surface was modeled as 3x2 super cells with dimensions a) 11.49 Å, b) 7.65 Å, and c) 18.98 Å, including the vacuum region with a thickness ca. 12 Å. The top three atomic layers of the slab as well as the adsorbates were allowed to relax. The bottom three atomic layers were held fixed at the bulk positions of ceria. Moreover, the transition states in possible dehydrogenation and steam reforming reaction processes were studied with the Nudged Elastic Band (NEB) method.

1. Dehydrogenation of ethanol

The adsorption energy of ethanol adsorbed on the surface (through the O of ethanol) was calculated to be -16.1 kcal/mol.

Moreover, we also calculated the possible dehydrogenation process upon this surface. The proposed possible subsequent pathways for dehydrogenation of ethanol on the 4Rh/CeO_2-(111) surface are schematically depicted in Scheme 1; the calculated corresponding potential-energy surfaces are drawn in Figure 1.

$$CH_3CH_2OH + surface \rightarrow CH_3CH_2OH_{(a)} \quad \triangle H = -16.1 \text{ kcal/mol}$$
$$CH_3CH_2OH_{(a)} \rightarrow CH_3CH_2O_{(a)} + H_{(a)} \quad \triangle H = 1.3 \text{ kcal/mol}$$
$$CH_3CH_2O_{(a)} + H_{(a)} \rightarrow CH_2CH_2O_{(a)} + 2H_{(a)} \quad \triangle H = -4.6 \text{ kcal/mol}$$
$$CH_2CH_2O_{(a)} + 2H_{(a)} \rightarrow CH_2CHO_{(a)} + 3H_{(a)} \quad \triangle H = -1.6 \text{ kcal/mol}$$
$$CH_2CHO_{(a)} + 3H_{(a)} \rightarrow CH_2CO_{(a)} + 4H_{(a)} \quad \triangle H = -14.8 \text{ kcal/mol}$$
$$CH_2CO_{(a)} + 4H_{(a)} \rightarrow CH_{2(a)} + CO_{(a)} + 4H_{(a)} \quad \triangle H = -20.3 \text{ kcal/mol}$$

Scheme 1. The possible reaction pathways for the dehydrogenation of ethanol on a 4Rh/CeO_2-(111) surface.

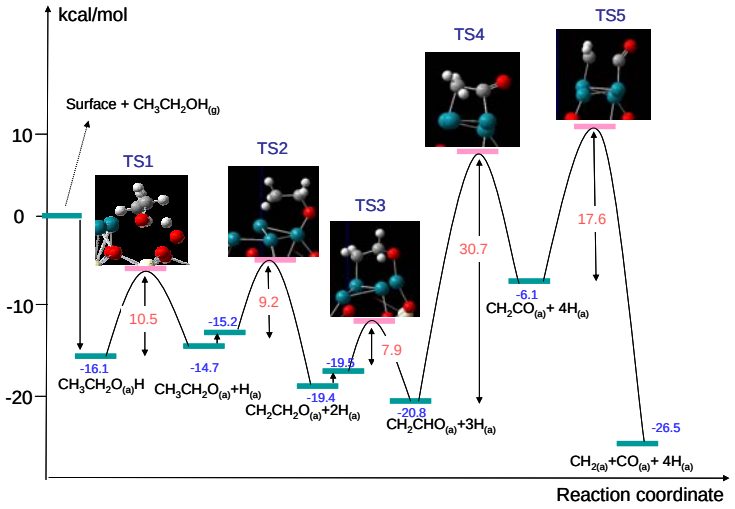

Figure 1. Calculated possible potential-energy diagram for the dehydrogenation of ethanol on the 4Rh/CeO_2(111) surface.

2. Steam reforming of CH_2 (CH_2+H_2O)

It is possible to carry out a steam reforming reaction of CH_2+H_2O to form more hydrogens. The proposed possible subsequent pathways are depicted in Scheme 2; the calculated corresponding potential-energy surfaces are drawn in Figure 2.

$CH_{2(a)} + H_2O_{(a)} \rightarrow CH_{2(a)} + OH_{(a)} + H_{(a)}$ $\triangle H = -4.0$ kcal/mol

$CH_2(a) + OH_{(a)} + H_{(a)} \rightarrow CH_{(a)} + OH_{(a)} + 2H_{(a)}$ $\triangle H = -6.8$ kcal/mol

$CH_{(a)} + OH_{(a)} + 2H_{(a)} \rightarrow CHOH_{(a)} + 2H_{(a)}$ $\triangle H = -4.9$ kcal/mol

$CHOH_{(a)} + 2H_{(a)} \rightarrow CHO_{(a)} + 3H_{(a)}$ $\triangle H = -31.2$ kcal/mol

$CHO_{(a)} + 3H_{(a)} \rightarrow CO_{(a)} + 4H_{(a)}$ $\triangle H = -43.5$ kcal/mol

Scheme 2. The possible reaction pathways for steam reforming of CH_2 on a 4Rh/CeO_2-(111) surface.

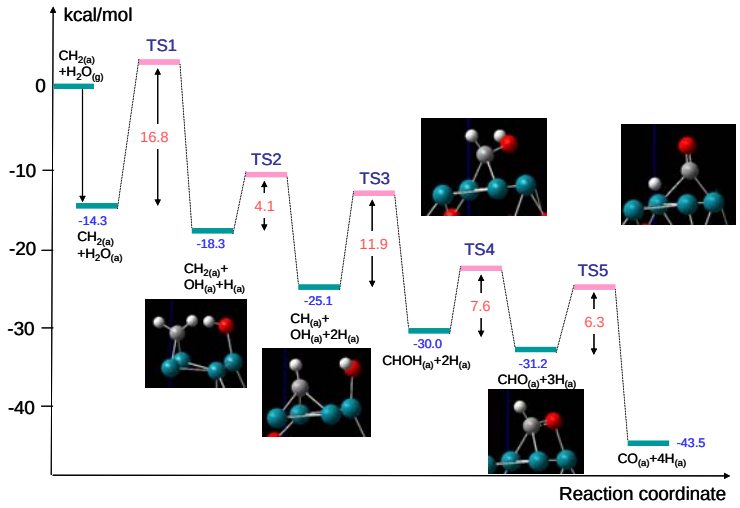

Figure 2. The calculated possible potential-energy surfaces for the steaming reforming of CH_2 on the surface of 4Rh/CeO_2(111).

3. Conclusion

The subsequent dehydrogenation of ethanol follows the processes starting the –OH group, then β-CH ,and α-CH, forming a four-membered ring intermediate CH_2CHO on the surface, and the barriers are 10.5, 9.2, and 7.9 kcal/mol, respectively. One more dehydrogenation of α-CH taking place to form CH_2CO (with barrier of 30.7 kcal/mol), then it breaks the C-C bond (17.6 kcal/mol of barrier) to form CH_2 and CO two separate subgroups absorbed on the surface. After further steam reforming of CH_2 with H_2O, the final adsorbed products of 2CO, and the total 8H

could be observed.

The dehydrogenation of second α -CH might be the rate-determined step of aforementioned reaction, since its calculated barrier height is 30.7 kcal/mol, the highest over all.

References:

1. H. L. Chen, S. H. Liu and J. J. Ho, J. Phys. Chem. B, 2006 , 110, 14816.
2. H. Idriss, Platinum Met. Rev., 200, 448, 105.
3. S. G. Wang, D. B. Cao, Y. W. Li, J. Wang and H. Jiao, J. Phys. Chem. B, 2006, 110, 9976.
4. S. G. Wang, X. Y. Liao, Jia. Hu, D.B. Cao, Y. W. Li, J. Wang and H. Jiao, Surf. Sci., 2007, 601, 1271.

(二) M. Hayashi（林倫年）：

In the past year, we first optimized the geometries of $Ce_{0.5}Zr_{0.5}O_2$ (111) surface and γ- Al_2O_3 (110) surface and then obtained the most probable adsorption sites of a 4Rh cluster or a Rh atom on the respective surfaces. We then investigated dehydrogenation of ethanol on 4Rh/ $Ce_{0.5}Zr_{0.5}O_2$ (111) surface and Rh/γ-Al_2O_3 (110) surface. A possible chemical reaction path for the dehydrogenation of ethanol was proposed for each surface system. Recently, we have been studying several transition state searching algorithms and a possible application of adaptive kinetic Monte Carlo simulation, combined with transition state theory, for chemical reactions taking place on a surface.

Geometry optimization and energy calculations were carried out based on Density functional theory. The exchange-correlation

functional was approximated by Perdew and Wang PW91[1] generalized gradient approximation (GGA) functional[2]. All calculations were performed using Vienna ab initio simulation program (VASP)[3-5] that uses plane-wave basis set and projected augmented wave (PAW) [6-7] for inner cores.

Geometry optimization for stable geometries was performed with the conjugate gradient algorithm (CG) method [8 and references therein]. For transition state search, nudged elastic band (NEB) method [8 and references therein] was used in which the energies of several "images" (7~8 images) were scanned. Each image was partially optimized by fixing the geometrical parameter related to the reaction and relaxing the rest. For both surfaces, the cutoff energy was set to 350eV or 400eV and the k points were $4\times4\times4$ for $Ce_{0.5}Zr_{0.5}O_2$ surface and $2\times2\times1$ for γ-Al_2O_3 (110) surface.

$Ce_{0.5}Zr_{0.5}O_2$ surface was constructed as follows; (1) CeO_2 crystal with Fm3m space group was constructed (lattice constants a = b = c =5.41Å); (2) since the ratio of the number of Ce atom to that of O atoms in the unit cell is C:O = 4:8, the number of Zr atoms in the unit cell was chosen such that Ce:Zr:O=2:2:8 and the structure was re-optimized and the resulting lattice constants were a = b = 5.285 Å and c=5.300 Å. A $3\times2\times1$ slab model for 2×3 $Ce_{0.5}Zr_{0.5}O_2$ (111) was then constructed by taking 6-layer from the optimized $Ce_{0.5}Zr_{0.5}O_2$. The dimension of the slab model was a = 7.4863 Å, b = 11.132 Å and c=18.5 Å. The c-axis has the vacuum layer. In the slab model, the atom positions of the lower 3 layers were fixed while the upper 3 layers were freely relaxed. A reaction mechanism of the dehydrogenation of ethanol on $Ce_{0.5}Zr_{0.5}O_2$ (111)

surface, $Rh/Ce_{0.5}Zr_{0.5}O_2$ (111) and $4Rh/Ce_{0.5}Zr_{0.5}O_2$ (111) was investigated based on the slab model.

A similar process was employed for γ-Al_2O_3 (110). The unit cell of monoclinic γ-Al_2O_3 crystal consists of about 40 atoms equivalent to $8Al_2O_3$. A slab model of γ-Al_2O_3 (110) was constructed with 8 layers in which the lower 3 layers were fixed and the rest free. 32 Al atoms and 48 O atoms were included in the slab model. The vacuum layer has 14 Å long along c-axis. The k points were set to $6\times4\times4$. A reaction mechanism of the dehydrogenation of ethanol on the slab model of γ-Al_2O_3 (110) surface was studied.

In these studies, LDA(GGA)+U was not taken into account.

1. Dehydrogenation of ethanol on $Rh/Ce_{0.5}Zr_{0.5}O_2$ (111) surface and $4Rh/Ce_{0.5}Zr_{0.5}O_2$ (111) surface

   The major difference in the optimized structures of the slab models of CeO_2 (111) and $Ce_{0.5}Zr_{0.5}O_2$ (111) surfaces is that the first layer of CeO_2 has a homogeneous Ce-O bond length of 2.34 Å while Ce-O and Zr-O bond lengths are distributed within 2.11 Å ~ 2.41Å. As a result, in $Ce_{0.5}Zr_{0.5}O_2$ (111) there exist many possible active sites that can adsorb ethanol molecules or Rh atoms upon deposition. Thus the first task is to determine the most probable adsorption site of ethanol on the slab model of $Ce_{0.5}Zr_{0.5}O_2$ (111) surface. It is found that the adsorption energy is -10.2 kcal/mol if adsorption takes place on Ce site and this is about 1.1 kcal/mol larger than Zr site. Once the H atom of the EtO(a)-H is dissociated and formed O-H bond on the surface, the

adsorption energy of EtO- becomes 46.0 kcal/mol while 18.7 kcal/mol is obtained for Zr site. We conclude that the most probable adsorption site of EtOH should be Ce site. For a Rh atom deposition, we find that if Rh is added at the middle of 3 Ce atoms with a slight displacement on the top layer the largest adsorption energy is obtained for Ce_2O (111) surface. For $Ce_{0.5}Zr_{0.5}O_2$ (111) surface, more serious displacement occurs forming 2.61 Å for Zr-O and 1.98 Å for Rh-O. We also consider 4Rh cluster adsorbed on $Ce_{0.5}Zr_{0.5}O_2$ (111) surface.

It is found that there are 9 intermediate products including 4 isomers and 6 transition states for one Rh adsorption. For the 4Rh deposition case, one more intermediate product is found. Table 1 lists the calculated barriers for the dehydrogenation of ethanol on these two surfaces. It is found that deposition Rh dramatically reduces C-C bond breaking energy while barriers for dehydrogenation do not show such a drastic effect. Table 2 presents adsorption energies of intermediate products. For 4Rh case, $C(a)H_2$-Rh and C(O)-Rh are found. The CO may remove an O atom from the surface and then form CO_2 to dissociate from the surface.

Table 1 Calculated barriers

	Barrier (kcal/mol)	
	1Rh	4Rh
O-H	15.1	15.2
C(α)-H	24.7	27.5
C(β)-H	22.7	26.9
C(α)-H (1st)	24.2	16.4
C(α)-H (2nd)	23.2	24.5
C-C	59.8	16.4

Table 2 Calculated adsorption energies of intermediate products

	Eads (kcal/mol)	
	1Rh	4Rh
CH_3CH_2O(H)-Ce	-10.8	-10.2
CH_3CH_2O(a)-Ce	-44.8	-63.3
Rh-C(a)H_2CH_2O(a)-Ce	-99.5	-106.6
Rh-C(a)H_2CHO	-65.4	-44.9
Rh-C(a)H_2C(a) O-Rh	-46.0	-40.5
H(a)-O	-101.5	--
C(a)H_2-Rh	--	--
C(O)-Rh	--	23.4

Our reaction mechanism of dehydrogenation of ethanol on 4Rh/ $Ce_{0.5}Zr_{0.5}O_2$ (111) surface can be summarized as follows:

(i) $CH_3CH_2OH \rightarrow CH_3CH_2O(a) + H(a)$

(ii-a) $CH_3CH_2O(a) \rightarrow CH_3CHO + H(a)$

(ii-b) $CH_3CH_2O(a) \rightarrow C(a)H_2CH_2O(a)+H(a)$

(iii) $C(a)H_2CH_2O(a) \rightarrow C(a)H_2CHO + H(a)$

(iv) $C(a)H_2CHO \rightarrow C(a)H_2C(a)O + H(a)$

(v) $C(a)H_2C(a)O \rightarrow C(a)H_2 + C(a)O$

The second step splits into two since removal of H can be started from C(α)-H or C(β)-H that produce aldehyde and oxametallacycle structure, respectively. The oxametallacycle structure leads to formation of $C(a)H_2$+CO(a) whose energy barrier requires only 16.4 kcal/mol. If $C(a)H_2$ removes 2 H atoms adsorbed nearby the C adsorption site, CH_4 can be easily formed. With stem reforming process, H_2 is produced by

(vi) $CH_4 + H_2O \rightarrow 3H_2 + CO$.

(vii) $CO + H_2O \rightarrow H_2 + CO_2$.

Over all reaction can then be $CH_3CH_2OH + 3H_2O \rightarrow 2CO_2 + 6H_2$.

Our calculation also indicates that CO(g) may remove an O atom from the surface and this may, in turn, form O vacancy as an additional reactive site on the surface. To treat this problem correctly, one should at least use LDA+U method to take into account a 4f electron that is generated by $Ce_2O_4 \rightarrow Ce_2O_3 + O$ type of reaction, in other words, Ce^{4+} obtains one electron in 4f orbital and form Ce^{3+}. It should be interesting to study chemical reactivity of O vacancy or defect site.

2. Dehydrogenation of ethanol on Rh/γ-Al_2O_3 (110) surface

We first identify adsorption site of Rh on γ-Al_2O_3 (110) surface. Figure 1 shows calculated Rh adsorption energies distribution mapped to the top view of the surface and geometry of the slab model of Rh/γ-Al_2O_3 (110) surface. In left panel of Fig.1 the adsorption energy is indicated by color green (small) to purple (large) via white.

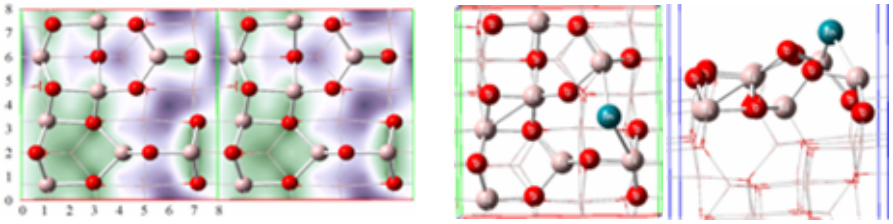

Figure 1. Left panel: view (2 × 1) of the PES for Rh adsorbed on the clear γ-Al_2O_3(110) surface. Right panel: The most stable structure of Rh loading.

We examine 6 possible cases for adsorption of ethanol: (i) cleanγ-Al_2O_3(110), (ii) bridge, (iii) OH, (iv) C(α), (v) C(β) and (vi) H. (ii) through (vi) are with Rh loading. Figure 2 shows the most probable and chemically interesting geometry of ethanol

adsorption. This adsorption can lead to ethanol dehydrogenation pathways. The others may promote dehydration of ethanol to ethylene.

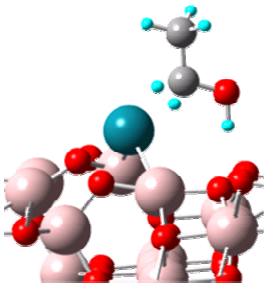

Figure 2. The most the most probable and chemically interesting geometry of ethanol adsorption

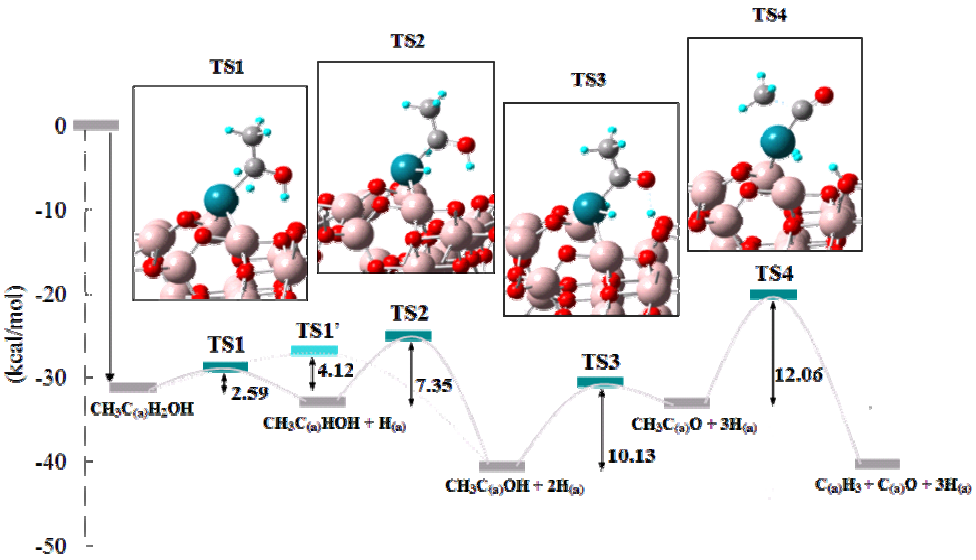

Figure 3. Reaction pathway for ethanol decomposition on Rh/γ-Al_2O_3(110) surface

In this configuration, ethanol adsorbed onto a Rh via α-Carbon, two α-hydrogen atoms from ethanol are first eliminated; the barriers for abstraction of the two α-hydrogen atoms are 2.59 an 7.35 kcal/mol. The hydrogenation continues with the loss of one hydrogen from the O-H, forming an intermediate species $CH_3C(a)O+3H(a)$, for which the successive barrier is 10.13

kcal/mol. Cleavage of the C-C bond occurs at this stage with a dissociation barrier E = 12.06 kcal/mol, to form $C(a)H_3$ + C(a)O + 3H(a).

Figure 3 shows a reaction pathway obtained from our calculations. There exist two pathways from $CH_3C(a)H_2OH$ to produce $CH_3C(a)OH$+2H(a); one is concerted pathway via TS1' directly going to the product and another is sequential pathway via intermediate species $CH_3C(a)HOH$ + H(a) via two transition states TS1 and TS2. Our result can be summarized as follows:

(i) $CH_3CH_2OH \rightarrow CH_3C(a)O + 3H \rightarrow$ (C-C cleavage) $\rightarrow CH_3$ + CO + nH

(ii) $CH_3CHO \rightarrow CH_3C(a)O + H \rightarrow$ (C-C cleavage) $\rightarrow CH_3$ + CO + nH

The results agree well with experimental results [9-11].

Transition states may differ because TS1' and TS2 structure yield zero and two imaginary frequencies. Correct geometries for TS1' and TS2 should be obtained in the near future. To this end, several transition state searching algorithms[8,12,13] are currently studied.

References:

1. J. P. Perdew, J. A. Chevary, S. H. Vosko, K.A. Jackson, M. R. Pederson, D. J. Singh and C. Fiolhais, Phys. Rev. B, 1992, 46, 6671.
2. J. A. White and D. M. Bird, Phys. Rev. B, 1994, 50, 4954.
3. G. Kresse, and J. Hafner, Phys. Rev. B, 1993, 47, 558.
4. G. Kresse and J. Furthmuller, Comp. Mater. Sci., 1996, 6, 15.

5. G. Kresse and J. Hafner, Phys. Rev. B, 1996, 54, 169.
6. P. E. Blochl, Phys. Rev. B, 1994, 50, 17953
7. G. Kresse and D. Joubert, Phys. Rev. B, 1999, 59, 1758.
8. F. Jensen, Introduction to Computational Chemistry, 2nd. Ed. Chap. 12, 2007 John Wiley & Sons Ltd. England.
9. M. Dömök, M. Tóth, J. Raskó and A. Erd o˝helyi, Appl. Catal. B, 2007, 69, 262.
10. H.-L. Chen, S.-H. Liu, J.-J. Ho, J. Phys. Chem. B, 2006, 110, 14816.
11. C. Hartnig, J. Grimminger, E. Spohr, Electrochim. Acta, 2007, 52, 2236.
12. http://theory.cm.utexas.edu/vtsttools/
13. A Heyden, A. T. Bell and F. J. Keil, J. Chem. Phys., 2005, 123, 224101.

(三) J. C. Jiang（江志強）：

Bio-ethanol is an important renewable energy carrier mainly produced from biomass fermentation. Besides operating conditions, the use of catalysts plays a crucial role in hydrogen production through ethanol reforming. A wide range of catalysts was tested, changing both the active phase (Rh, Pt, Pd, Ru, Ni, Cu, Zn, Fe) and the oxide support (Al_2O_3, 12%CeO_2–Al_2O_3; CeO_2; CeO_2–ZrO_2; ZrO_2).[1] The reaction pathways and thermodynamics of ethanol steam reforming have been studied extensively recently.[2–6] It can be seen that hydrogen production varies significantly with different reaction pathways. The selection of proper support for catalyst and the methods of catalyst preparation significantly affect

the activity of catalysts. Rh and Ni are so far the best and the most commonly used catalysts for ethanol steam reforming towards hydrogen production. Previous reports [7, 8] have been proven that Cu has the excellent performance for water gas shift reaction. As Rh and Ni are inactive for water gas shift reaction, the development of bimetallic catalysts, alloy catalysts, and double-bed reactors is promising to enhance hydrogen production and long-term catalyst stability. Based on economic point of view, the investigation of the reaction mechanism of ethanol steam reforming (ESR) over the Ni-Cu/α-Al_2O_3 surface is our endeavor in the past year. We considered two stages of ESR reaction; first is the ethanol dehydrogenation over the Ni /α-Al_2O_3 surface, then the WGS reaction on Cu/α-Al_2O_3 surface.

In this report, we divide into three parts: the first is "CO oxidation on Cu cluster"; the second is "WGS on Cu/α-Al_2O_3 surfaces"; and the final is "Ethanol dehydrogenation on α-Al_2O_3 surface". The study of "The ethanol dehydrogenation on the Ni /α-Al_2O_3 surface" has not been completed.

Computational Method

All calculations were performed using spin polarized DFT within the generalized gradient approximation (GGA) as implemented in the Vienna ab initio simulation package. In our calculations, electron-ion interactions were described by ultrasoft pseudo-potentials and the PW91 exchange correlation functional was used. The Monkhorst-Pack scheme was used to generate k-points. The cutoff energy for the plane waves was 300 eV, and the Monkhorst-Pack set of four k points was used. Structural

minimizations were performed using a conjugated gradient technique in which the iterative relaxation of atomic positions was stopped when the change in the total energy between successive steps was less than 0.001 eV. For a chemical reaction of given reactants and products, the minimum energy path is found via the NEB method by performing a restrained minimization of a series of images on the 3*N*-dimension potential energy surface. The harmonic restraints between adjacent NEB images prevent the collapse of all of the NEB images to the given local minima (namely, the reactants or the products) and ensure that the paths found are indeed the minimum energy paths.

1. CO oxidation on Cu cluster

Cu growth on alumina surfaces has been experimentally studied using both native surfaces of α-alumina and thin films of aluminum oxide grown on metallic substrates. The results concerning Cu deposition have been found to be contradictory.[9-11] Their results provided direct evidence for the 3D clustering of copper on the reconstructed face above a coverage of 0.3 ML. Cu clusters form islands of 3-8 Å in height and 20-30 Å in diameter; these islands are randomly distributed on the surface. However, it was not possible to image copper at coverage lower than 0.3 ML; the possibility that small 2D islands of copper are formed prior to the 3D clusters could not be ruled out. Therefore, we considered the investigations both CO oxidation on Cu cluster and on the coverage at 1/3 - 4/3 ML of Cu on alumina. The latter case will be presented at the next part.

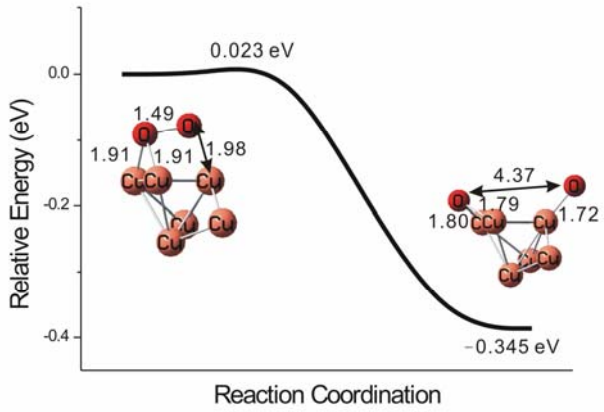

Figure 1. Potential energy surface for the decomposition of oxygen molecule on Cu cluster.

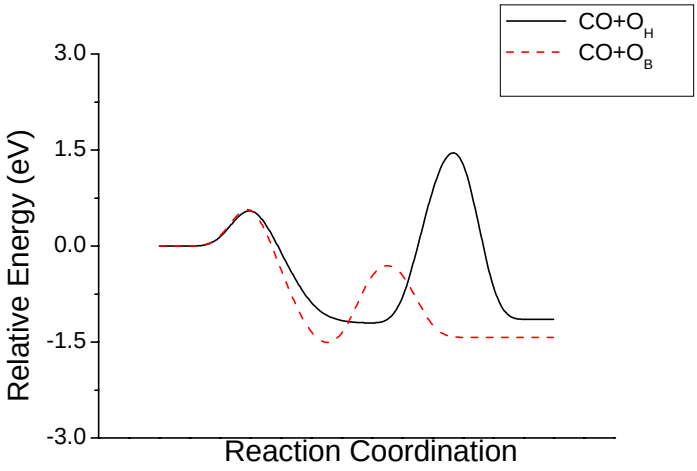

Figure 2. Potential energy surfaces for CO oxidation with oxygen atom at bridge and hollow sites.

As shown in Figure 1, we can find the decomposition of O_2 on Cu cluster is almost barrierless. The absorbed CO can be oxidized with the $O_{(abs)}$ atom. Figure 2 demonstrates the barrier of CO oxidation with O_B (1.17 eV) is much lower than that with O_H (2.68 eV).

2. WGS on Cu/α-Al_2O_3 surfaces

Aluminum oxide (Al_2O_3) is a particularly important substrate for

catalysis purposes because of both its mechanical and thermal resistance. To date, the most studied phase of Al_2O_3 is the stable α phase. This is presumably due to the stability and the less complex structure of this phase, as compared to the metastable aluminas. In this part, WGS reaction via redox, carboxyl and formate mechanisms has been studied on five different systems: bare α-Al_2O_3 (0001) surface; 1/6 ML Cu/α-Al_2O_3 surface; 4/3 ML Cu/α-Al_2O_3 surface; Cu-3H_2O /α-Al_2O_3 surface and Cu/Hydroxylated α-Al_2O_3 surface. In addition, we also examined the CO oxidation with O_2 on Cu/α-Al_2O_3 at the coverage at 4/3 ML of Cu.

Our calculated results indicated that except Cu/α-Al_2O_3 catalyst, which carboxyl mechanism is the most favorable pathway with higher energy barrier (1.94 eV), redox mechanism is the most favorable of WGS on Cu/α-Al_2O_3 surfaces. As shown in Figure 3, The barrier (0.89 eV) of H_2 desorption is very close to the barrier (0.91 eV) of the determined state - CO oxidation to CO_2. As the increasing the H_2O coverage, the barrier of

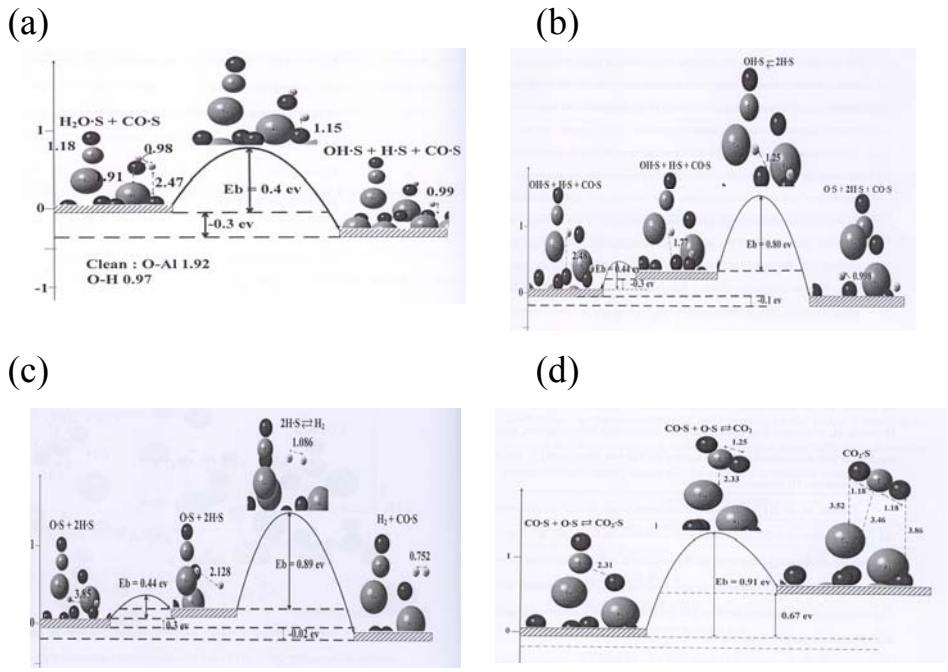

Figure 3. WGS reaction potential energy surfaces from NEB calculations (a) $H_2O_{(a)} \rightarrow OH_{(a)} + H_{(a)}$; (b) $OH_{(a)} \rightarrow O_{(a)} + H_{(a)}$; (c) $2H_{(a)} \rightarrow H_{2(g)}$ and (d) $CO_{(a)} + O_{(a)} \rightarrow CO_{2(g)}$ on Cu/α-Al_2O_3 (0001) surface at Cu coverage of 1/6 ML via redox mechanism.

3. Ethanol dehydrogenation on α-Al_2O_3 surface

The major aim of this study is to find the efficient and economic catalyst system for ethanol steam reforming (ESR). Initially, we planed to study the dehydrogenation of ethanol on Ni/α-Al_2O_3 surface and WGS reaction on Cu/α-Al_2O_3 surface to evidence the Ni-Cu/α-Al_2O_3 catalyst system has to potential for ethanol steam reforming and to understand the reaction mechanism of ethanol steam reforming on Ni-Cu/α-Al_2O_3 catalyst system.

The above result indicated the low coverage of the copper deposition on Al_2O_3 is a potential catalyst system for WGS reaction. We were curious about does the ethanol steam reforming on the bare α-Al_2O_3 surface? The ethanol steam reforming on the bare α-Al_2O_3 surface might be via dehydrogenation or dehydration pathway.

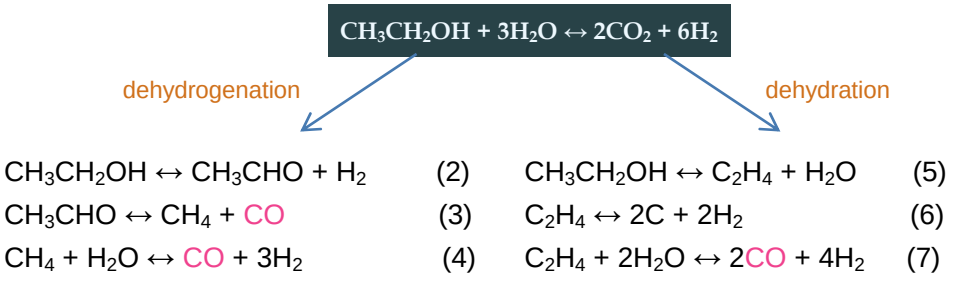

Our results indicated that the dehydrogenation via the O-H scission is reaction with the lowest barrier (0.81 eV), but the further reactions become unfavorable, since the barriers were close to 2 eV, whereas the dehydration is the favorable pathway (figure 4), which is in good agreement

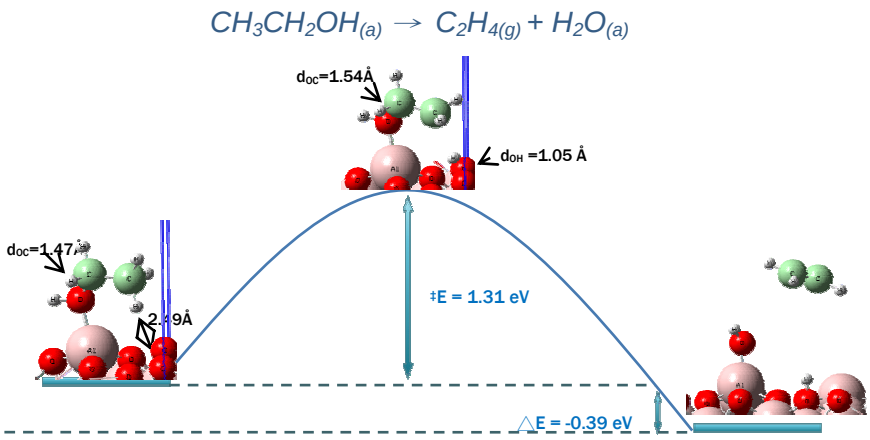

Figure 4. Potential energy diagram from NEB calculation for ethanol dehydration to ethylene on clean α-Al_2O_3 (0001) surface.

with the experimental observation.[12] Therefore, the bare α-Al_2O_3 surface is poor catalyst for ethanol steam reforming, it'll cause the coke formation.

References:

1. Aupretre F, Descorme C, Duprez D., Catal. Commun., 2002, 3, 263.
2. Freni S, Maggio G, Cavallaro S., J Power Sources 1996, 62, 67.

3. Ioannides T., J Power Sources, 2001, 92, 17.
4. Benito M, Sanz JL, Isabel R, Padilla R, Arjona R, Daza L., J. Power Sources, 2005, 151, 11.
5. Vaidya PD, Rodrigues AE., Chem. Eng. J., 2006, 117, 39.
6. Fatsikostas AN, Verykios XE., J. Catal., 2004, 225, 439.
7. J. Nakamura, I. Nakamura, T. Uchijima, Y. Kanai, T. Watanabe, M. Saito and T. Fujitani, J. Catal., 1996, 160, 65
8. N. Schumacher, A. Boisena, S. Dahl, A.A. Gokhale, S. Kandoi, L.C.Grabow, J.A. Dumesic, M. Mavrikakis and I. Chorkendorff, J. Catal., 2005, 229, 265.
9. Y. Wu, E. Garfunkel and T. E. Madey, J. Vac. Sci. Technol. A, 1996, 14, 1662.
10. J. G. Chen, M. L. O. Colaianni, W. H. Weinberg and J. T. Yates, Surf. Sci., 1992, 279, 223.
11. F. S. Ohuchi, R. H. French, R. V. Kasowski, J. Appl. Phys., 1987, 62, 2286.
12. C. V. Ovesen, B. S. Clausen, B. S. Hammershoi, G Steffensen, T. Askgaard, I.Chorkendorff, J. T. Norskov, P. B. Rasmussen, P. Stoltze and P. Taylor, J. Catal, 1996, 158, 170.

二、Si-quantum dots:

(一) B. C. Wang（王伯昌）：

In the simulations, both deposition and diffusion of adatoms on the substrate surface are considered as elementary processes. In this study, we investigated the diffusion length of adatoms and neglected the adsorptions from the surface. A 100x100 lattice was used as the basic substrate, which can be treated as one step, and

this substrate can be further divided into several steps with equal width, including 2 steps (50 atoms per step)、4 steps (25 atoms per step)、5 steps (20 atoms per step)、10 steps (10 atoms per step) and 20 steps (5 atoms per step). The deposition rate is set as 0.7 monolayer per second (ML/sec). The deposition time is one second and therefore the total deposition atoms are only 7000 atoms. Because the thickness in each step is only one monolayer, the SOS model [22-28] can be used as the simulated system without defect. This substrate system can simulate a simple cubic crystal with a regular facet [100]. Periodic boundary condition is applied along the x-axis and y-axis in the model, with the step-flow direction as y-axis.

The growth process is described by random deposition on the substrate with a constant rate. The transition rate for a diffusion process from lattice site *i* to *j* is assumed to be

$$\nu = \nu_0 \exp\left(E_A^{ij} \Big/ k_B T \right) \qquad (1)$$

The diffusion rate of adatoms is assumed as Arrhenius type, where ν_0 is the atomic vibration frequency which is assigned as

$$\nu_0 = \left(2K_B T\right) \Big/ h \qquad (2)$$

where T is the substrate temperature and k_B is Boltzmann constant. The activation energy E_A^{ij} is determined by a bond counting scheme with

$$E_A^{ij} = E_S + nE_N + E_{step} \qquad (3)$$

where E_S is the surface potential; n and E_N are the number of the nearest neighbors and the binding energy between any two nearest neighbors, respectively. E_{step}, so-called step-edge barrier, is the

anisotropic diffusion (iES barrier) for an atom hopping from the current step to the edges of the upper step. The typical semiconductor parameters [3] is set as $E_S = 1.0eV$, $E_N = 0.25eV$ and $E_{step} = 0.15eV$, respectively. By adjusting the step-edge barrier, we can describe the asymmetric step-edge barrier suggested by Schwoebel et al [29-30].

The diffusion length (R) can be estimated by Einstein diffuse equation in homogeneous diffusion.

$$R^2 = Dt \qquad (4)$$

where D is diffusion coefficient with the unit (length^2/Sec) and t is the time elapse between two consecutive atomic deposition events. The diffusion coefficient can be calculated by $D = A\nu_0 \exp\left(-E_A/kT\right)$ where $A = n_x \cdot n_y \cdot a^2$, and n_x and n_y are the average diffusion distance along x and y axes and a is the lattice constant.

In order to characterize the surface morphology of step-flow growth, two analytical methods are used to discuss the simulation results: step growth coverage (SGC) and step-flow analysis. The SGC can be expressed as

$$SGC = N_{step} / N_{total} \qquad (5)$$

where, N_{total} is total numbers of deposition atoms and N_{step} is the number of atoms flowing across steps boundaries. Step-flow analysis includes two parameters, average step-flow layer (SFL) and step-flow ratio (SFR), to characterize the pattern formed by the adatoms on the step edges. SFL describes the average number of layers per step, formed through the step-flow growth. SFL and SFR are defined as

$$SFL = N_{step} / (number\ of\ steps \times L_x) \qquad (6)$$

$$SFR = SFL / step\ width \qquad (7)$$

where L_x is the width of the subtract in x direction. By combining the SFL with the width of step, SFR represents average step-flow covering, i.e., the expansion ratio for each step as shown in Eq. (7).

Main discoveries

In order to investigate the variation in the diffusion length (R) of adatoms, which induces the change in surface morphology, we studied the temperature and step-width effects, and summarized these two effects with a phase diagram.

1. Temperature effect:

   By comparing the diffusion length (R) with half of step width (L/2, L is step width), we can elucidate the relation between temperature effect and surface growth mode. We roughly divide temperature range into three regions including T1 region (300K~500K), T2 region (500K~750K) and T3 region (750K~1000K) according to the growth morphology. In the simulation scheme, the temperature parameter is implemented in the Arrhenius equation which is used to calculate the diffusion rate. When temperature raises, the average kinetic energy of adatoms increases; the diffusion rate and length of adatoms also increase and therefore the adatoms can diffuse to a more stable position with more neighboring adatoms. If temperature is high enough, the adatoms with large R can easily diffuse from the initial deposition position to the step-edge and enhance the step-flow. From the Arrhenius and Einstein diffusion equation

(Eq. 4), *R* is dependent only on temperature and therefore we can investigate the temperature effect on step-flow growth through the relationship between the SGC and *R*, since *R* depends only on temperature. The results are listed in Table 1. Since L/2 can be used to characterize the range of homogeneous diffusion, we can further explore the temperature effect through the relationship between *R* and L/2 with the results of SGC simulation.

TABLE 1: Temperature dependence of the *SGC* and *R* values with various step- widths.

SGC* & *R **Temp**	***R* value**	**2 steps L/2=25 *SGC***	**4 steps L/2=12.5 *SGC***	**5 steps L/2=10 *SGC***	**10 steps L/2=5 *SGC***	**20 steps L/2=2.5 *SGC***
300K	0	0	0	0	0	0
350K	0.01	0	0	0	0	0
400K	0.05	0	0	0	0	0
450K	0.26	0	0	0	0	0
500K	0.99	0	0	0	0.01	0.15
550K	2.99	0	0	0.04	0.11	0.46
600K	7.45	0	0.14	0.21	0.33	0.65
650K	16.52	0.19	0.45	0.49	0.62	0.79
700K	32.44	0.42	0.63	0.68	0.75	0.85
750K	58.36	0.61	0.78	0.83	0.86	0.88
800K	97.75	0.71	0.83	0.86	0.88	0.90
850K	154.36	0.81	0.86	0.89	0.89	0.92
900K	232.10	0.87	0.89	0.90	0.91	0.92
950K	334.78	0.89	0.91	0.91	0.92	0.92
1000K	466.15	0.91	0.92	0.92	0.92	0.92

As listed in Table 1, it shows that the SGC values increase as temperature increases. When temperature belongs to T1 region (300K~500K), most of the adatoms stay at the original random deposition site due to lack of enough kinetic energy to diffuse and

therefore the morphology belongs to random deposition growth. When temperature raises gradually to T2 region (500K~750K), the *R* of adatoms increases accordingly and homogeneous diffuse appears. The step-flow appears only when *R* is compatible to L/2 for systems with narrow step-width in T2 region. The step-flow morphology becomes apparent because that around 750K there are over 50% (SGC > 0.5) of adatoms diffusing to the step-edge. When L/2 decreases with temperature fixed the *SGC* increases. When temperature belongs to T3 region (750K~1000K), *R* is longer than the largest step-width in our models (50 atoms per step), and the SGC increases substantially over 50%. When temperature reaches 1000K, there are over 90% of adatoms contributing to step-flow growth and the surface morphology is composed entirely by step-flow growth.

The SGC values are almost close to zero when L/2 is larger than *R* value and the SGC values become substantial if L/2 is equal or smaller to *R* value. The increasing of the SGC value can be used to depict the onset of step-flow growth. Thus, the growth mode can be characterized according to relation between *R* and L/2, as shown in the following.

$R \le 1$: Morphology proceeds with random deposition mode;

$1 < R < L/2$: Morphology proceeds with island mode;

$R \ge L/2$: Morphology proceeds with step-flow mode.

When $R \le 1$, most of the adatoms stay at the initial random deposition site. When $1 < R < L/2$, the adatoms tend to diffuse around within the step terrace, and step-flow growth is not

pronounced. But when $R \geq L/2$, the diffusion length can cover the entire step-width, so the adatoms tend to attach to the step-edge and the step-flow growth become apparent. As a result, the step-flow growth becomes the dominant growth mode. The SGC results of these simulations are plotted in Fig. 4. In T1 region (below 500K), the value of SGC is close to zero and R of adatoms is smaller than L/2 due to low kinetic energy and only few adatoms near the step-edge. As shown in Table 1, diffusion lengths are smaller than 1 when temperature is below 500K. With $R \leq 1$, the adatoms are unable to diffuse on the surface and this makes the surface morphology mainly composed by random deposition growth. As temperature increases over 500K, the adatoms start to aggregate around the step-edge and the pattern of the step-flow growth emerges.

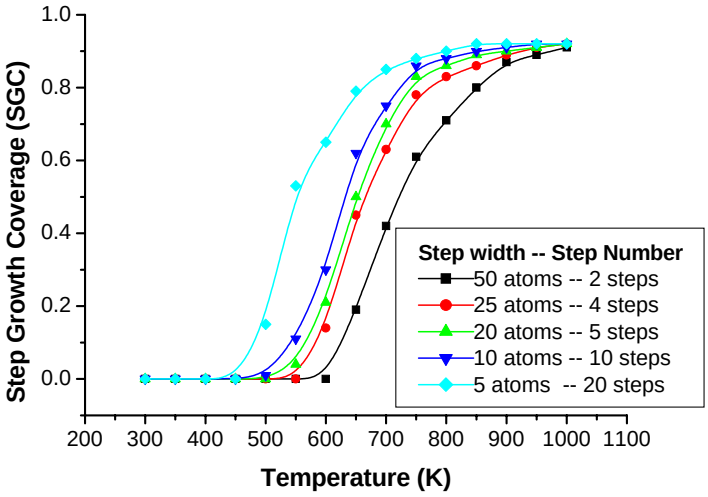

Figure 4. Temperature effect of *SGC* for various step widths with an inverse ES barrier.

2. Step width effect:

From the above discussion, it is found that the ratio between *R*

and L/2 can determine the pattern of surface morphology. Since R is only dependent on temperature (Eq. 4), one can characterize the step-width of the substrate with a transition temperature (T_c) for the onset of step-flow growth, i.e., when R is equal to the L/2, as shown in the previous section. The relation between the T_c and L/2 for all simulation models are shown in Table 3. It is found that the model with narrow step-width corresponds to low T_c. With narrow step-width, the adatoms can easily aggregate to the outer step-edge through homogeneous diffusion, and make the onset of step-flow growth appear even in low temperature. Therefore, T_c is low for the model with narrow step width (T_c= 537K, for step width: 5 atoms). However, with wide step-width, the aggregation through island growth on the terrace competes with the cluster formation around the step-edge and therefore temperature has to increase to allow the adatoms to diffuse far enough to be able to attach the outer step-edge. For example, T_c is 676K for substrate with 50 atoms as step-width, and T_c is 572K for substrate with 10 atoms as step-width.

As shown in Figure 5, the SGC decreases as the step width increases at almost all the temperature. It is interesting to note that the step-width effect is not pronounced in T1 and T3 regions. In T2 region, the step-flow growth is strongly influenced by step width. By combining the simulation results in Fig. 5 with T_c in Table 2, it is found that when temperature is larger than T_c, step-down mass current appears and the step-flow growth begin. In T2 region, the T_c increases as the step-width increases. When temperature is larger or lower than T_c, the trend of SGC is not

evident and this indicates that the surface growth mode is not influenced by the step-width effect in these temperature regions. The influence of the step-width effect becomes noticeable on surface growth mode when temperature is in T2 region since the transition temperatures of all the studied models in T2 region. It is because that the surface growth pattern is determined by the competition between the island formation and step-flow growth in this temperature region and therefore it is rather sensitive to the variation of step-width. In order to demonstrate the extent of step-flow growth influenced by step-width effect, we compare the SFR with various step widths as shown in Table 2.

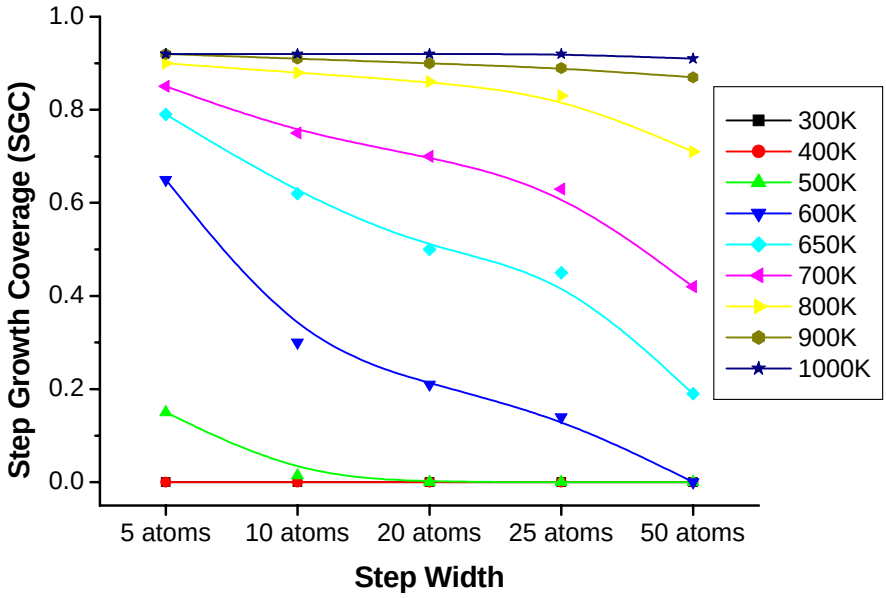

Figure 5. Step-width effect of step growth coverage (*SGC*) in various temperatures with an iES barrier.

TABLE 2. Temperature dependence of the step-flow layer (*SFL*) (layers) and step-flow ratio (*SFR*) (%) for various step widths.

	2 steps		**4 steps**		**5 steps**		**10 steps**		**20 steps**	
	SFL	***SFR***	***SFL***	***SFR***	***SFL***	***SFR***	***SFL***	***SFR***	***SFL***	***SFR***
	Layer	(%)	Layer	(%)	Layer	(%)	Layer	(%)	Layer	(%)
300K	0	0	0	0	0	0	0	0	0	0
350K	0	0	0	0	0	0	0	0	0	0
400K	0	0	0	0	0	0	0	0	0	0
450K	0	0	0	0	0	0	0	0	0	0
500K	0	0	0	0	0	0	0.10	1	0.53	11
550K	0	0	0	0	0.56	3	0.80	8	1.61	32
600K	0	0	2.45	10	2.94	15	2.10	21	2.28	46
650K	6.65	13	7.79	31	7.00	35	4.34	43	2.77	55
700K	14.71	30	11.05	44	9.80	49	5.52	55	2.98	60
750K	21.35	50	13.65	55	11.62	58	6.02	60	3.08	62
800K	24.85	43	14.53	58	12.04	60	6.16	63	3.15	63
850K	28.00	56	15.05	60	12.46	62	6.32	63	3.22	64
900K	30.45	61	15.51	62	12.60	63	6.37	64	3.22	64
950K	31.85	62	15.93	64	12.74	64	6.44	64	3.22	64
1000K	31.85	64	16.12	64	12.88	64	6.44	64	3.22	64

3. Phase diagram discussion:

Combining the results of previous two sections, we constructed a phase diagram (see Fig. 6 for details) to explain the surface growth mode. We divided the phase diagram into three different regions according to SGC value: Region I (SGC: 0~0.125), Region II (SGC: 0.125~0.87) and Region III (SGC: 0.87~1). The surface growth mode in Region I belongs to random deposition growth. Judging from simulated morphology shown in Fig. 7 (300K), the deposition growth is the dominant mode in Region 1 and surface growth pattern shows minimal influence by either temperature or step-width effects. In Region III, the surface growth mode belongs to step-flow growth and is not influenced

by either temperature or step-width effects. As a result, we can conclude that the surface growth mode is not affected by step-width effect when temperature belongs to T1 and T3 regions.

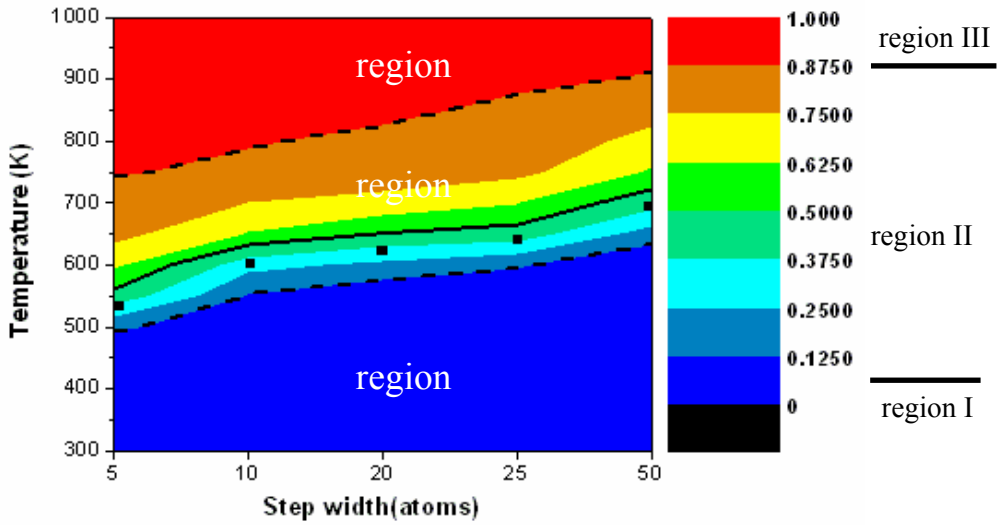

Figure 6. Temperature-step width diagram for surface growth mode with *SGC* in color scale (2D diagram). The regions are separated by black dot lines. Region I belongs to random deposition growth and Region III is dominated by step-flow growth. The surface growth mode of region II represents the transition from random deposition growth to step-flow growth and is strongly influenced by the temperature and step width. The black dots below the black curve represent the T_c point.

	300K	**650K**	**1000K**
2-step	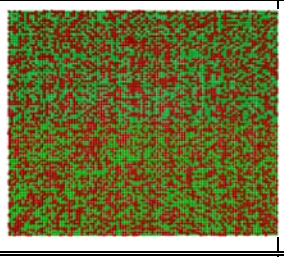	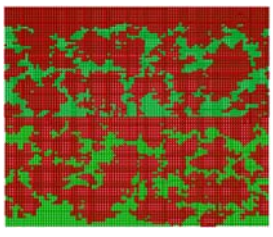	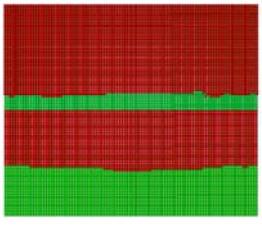
4-step	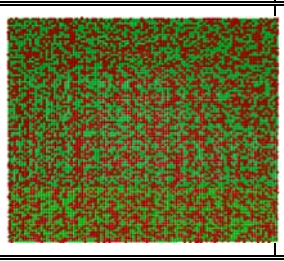	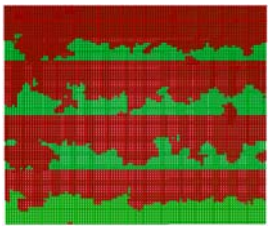	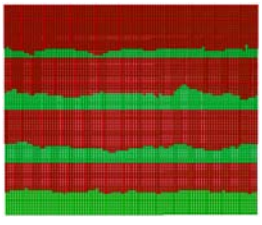

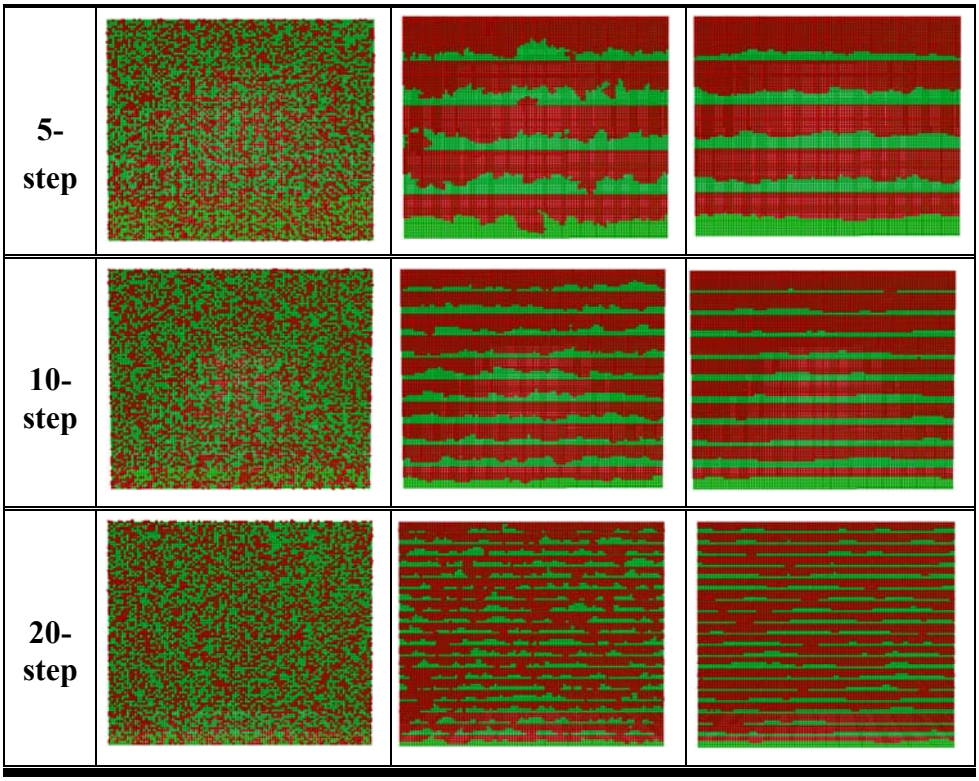

Figure 7. Top view of the simulated morphology with an iES barrier for various step-widths and temperatures.

Comparatively, the SGC varies at Region II as shown in Figure 6. The Region II represents the transition from random deposition growth to step-flow growth. The black curve in Region II represents the SGC = 0.5. The black dots below the black curve represent the T_c points. The results show that T_c increases as step-width increases. The black curve of SGC rises slowly as step-width increases. Generally speaking, by increasing temperature or decreasing step-width, the surface morphology is dominated by step-edge aggregation and this in turns makes the step-flow growth apparent.

TABLE 3: Step-width effect on the transition temperature (T_c).

steps / Temp	**2 steps L/2=25**	**4 steps L/2=12.5**	**5 steps L/2=10**	**10 steps L/2=5**	**20 steps L/2=2.5**
$\boldsymbol{T_c}$	676K	628K	614K	572K	537K

Conclusion

We successfully analyzed the influence of temperature and step-width on the surface growth pattern of a semiconductor-like uniform-spacing stepped model with inverse Ehrlich-Schwoebel (iES) barrier. The relation between diffusion length (R) and half of step-width (L/2) is constructed to estimate the T_c in order to predict the growth mode on the surface. A step width-temperature diagram was employed to characterize the surface growth mode into three regions, i.e., random deposition growth, step-flow growth and transition between these two growth modes, according to the step growth coverage and T_c. It is found that the step-width effect has great influence on surface growth mode in the transition region. Our results not only shed a light on understanding the surface morphology controlled by the temperature and substrate topology, but also provide a simple way to predict the surface growth mode, which is crucial for the thin film growth process.

References:

1. H. Minoda, Thin Solid Film, 2003, 424, 40.
2. A. V. Latyshev, A. L. Aseev, A. B. Krasilnikov, S. I. Stenin, Surf. Sci., 1989, 212, 157.
3. J. Mysliveček, C. Schelling, G. Springholz, F. Schäffler, B. Voigtländer, P. Smilauer, Materials Science and Engineering B, 2002, 89, 410.

4. J. Mysliveček, C. Schelling, F. Schäffler, G. Springholz, P. Smilauer, J. Krug, B. Voigtlander, Surf. Sci., 2002, 520, 193.
5. B. Voigtländer, T. Weber, P. Smilauer, D. E. Wolf, Phys. Rev. Lett., 1997, 78, 2164.
6. W. K. Burton, N. Cabrera, F. C. Frank, Trans. R. Soc. A, 1951, 243, 299.
7. T. Maroutian, L, Douillard, H. Ernst, J. Phys. Rev. B, 2001, 64, 165401.
8. B. J. Gibbons, S. Schaepe, J. P. Pelz, Surf. Sci., 2006, 600, 2417.
9. H. Omi, T. Ogino, Thin Solid Films, 2000, 380, 15.
10. Z. M. Wang, L. Däweritz, K. H. Ploog, Surf. Sci., 2000, 459, L482-L486.
11. P. Tejedor, F. E. Allegretti, P. Smilauer, B. A. Joyce, Surf. Sci., 1998, 40, 82.
12. M. A. K. Zilani, H. Xu, X.-S. Wang, A. T. S. Wee, Appl. Phys. Lett., 2006, 88, 023121.
13. R. L. Schwoebel, E. J. Shipsey, J. Chem. Phys., 1966, 37, 3682.
14. G. S. Bales, A. Zangwill, Phys. Rev. B, 1990, 41, 5500.
15. D. Vilone, C. Castellano, P. Politi, Surf. Sci., 2005, 588, L227-L232.
16. J. M. Pomeroy, J. Jacobsen, C. C. Hill, B. H. Cooper, J. P. Sethna, Phys. Rev. B, 2002, 66, 235412.
17. M. Krishnamurthy, M. Wassermeier, D. R. M. Williams, P. M. Petroff, Appl. Phys. Lett., 1993, 62, 1922.
18. P. Tejedor, P. Smilauer, C. Roberts, B. A. Joyce, Phys. Rev. B,

1999, 59, 2341.
19. F. Nita, A. Pimpinelli, Phys. Rev. Lett., 2005, 95, 106104.
20. T. Frisch, A. Verga, Phys. Rev. Lett., 2005, 94, 226102.
21. H. Omi, Y. Homma, Phy. Rev. Lett., 2005, 95, 216101.
22. J. D. Weeks, G. H. Gilmer, K. A. Jackson, J. Chem. Phys., 1976, 65, 712.
23. C. Olesky, Surf. Sci., 2004, 549, 246.
24. D. B. Abraham, V. Mustonen, A. J. Wood, J. Phys. A: Math. Gen., 2004, 37, L233.
25. H. J. W. Zandvliet, R. V. Moere, B. Poelsema, Phys. Rev. B, 2003, 68, 073404.
26. S. Dieluweit, H. Ibach, M. Giesen, T. L. Einstein, Phys. Rev. B, 2003, 67, 121410(R).
27. S. C. Park, J. M. Park, Phys. Rev. E, 2003, 67, 010103(R).
28. S. C. Park, J. M. Park, D. Kim, Phys. Rev. E, 2002, 65, 036108.
29. R. L. Schwoebel, E. J. Shipsey, J. Appl. Phys., 1969, 40, 614.
30. K. Kyuno, G. Ehrlich, Surf. Sci., 1997, 394, L179.

三、InN/TiO_2 related calculations:

(一) M. C. Lin（H. T. Chen 陳欣聰）：

Density Functional Study on the Electronic Properties of the InN/TiO_2 Solar Cell Using the Linker Molecules –OY(O)O–, Y=B, P:

In order to explain the robust inorganic linkers (such as –OY(O)O–, Y=B, P) for semiconductor quantum dot TiO_2 solar cell, we have applied the Vienna Ab Initio Program (VASP)

package to study the electronic structures and densities of states (DOS) of the modifiers InN/TiO_2 using the linker molecules. The calculations were performed using DFT and a plane-wave basis set with the ultra-soft Vanderbilt pseudopotentials (US-PP). The exchange-correlation functions were treated with the generalized gradient approximation (GGA) of the Perdew-Wang (PW91) functional. The Brillouin zone was sampled with the Monkhorst - Pack grid. The calculations were carried out using (4×4×1) Monkhorst-Pack mesh k-points. Also, we used a 600 eV cut-off energy, which allows convergence to 0.01 eV in the total energy.

The computed lattice parameters for the anatase (101) surface are a = 3.785 Å, c = 10.239, and the internal coordinate, c = 0.201, while those for the rutile (110) surface are a = 4.593 Å, c = 2.933, and c = 0.296. Those parameters are in good agreement with the experimental values as well as with other theoretical values. The calculated band gaps are 2.2 and 1.8 eV for the anatase and rutile surfaces, respectively, which are significantly smaller than the experimental values (3.2 eV for anatase and 3.0 eV for rutile) due to the DFT calculations. Therefore, the scissors operators of 1.0 and 1.2 eV for the anatase and rutile surface were applied to obtain results consistent with the experimental values, as well as for the following calculations.

First we calculated the structures and adsorption energies of –OY(O)O–, Y=B, P adsorbed on TiO_2 anatase surface. Our results show that the bonding energy of –OB(O)O– on TiO_2 (56.9 kcal/mol) is stronger than that of –OP(O)O– on TiO_2 (29.2 kcal/mol). Then we studied the $(InN)_x$, x= 1~3, adsorbed on

OY(O)O–TiO_2, Y=B, P. It was found the binding energies of $(InN)_x$ adsorbed on –OB(O)O–TiO_2 are larger than those of $(InN)_x$ on –OP(O)O–TiO_2. The predicted energies are 69.2~79.9 kcal/mol for –OB(O)O–TiO_2, whereas they are 52.4~62.9 kcal/mol for –OP(O)O–TiO_2. In addition, we calculated the electronic properties for those structural models.

As shown in Figure 1, the adsorbed –OY(O)O–, Y=B, P cause the reduction of the band gap from 3.2 eV to 2.7 eV for anatase surface to provide the possibility of photoexcitation at the 2.7 eV (459 nm) within the UV/Vis light region. The band gap lowering and red shift of the absorption edge are found to increase as the number of InN increases. The density of states (DOS) are shown in Figure 2. By analyzing the density of states (DOS), the presence of the –OB(O)O– density of state localizes slightly above the upper edge of the valence band, while the –OP(O)O– density of states localizes below the upper edge of the valence band as well as the overlap of the InN and the –OB(O)O– in the valence band is more significant than that of the InN and the –OP(O)O–.

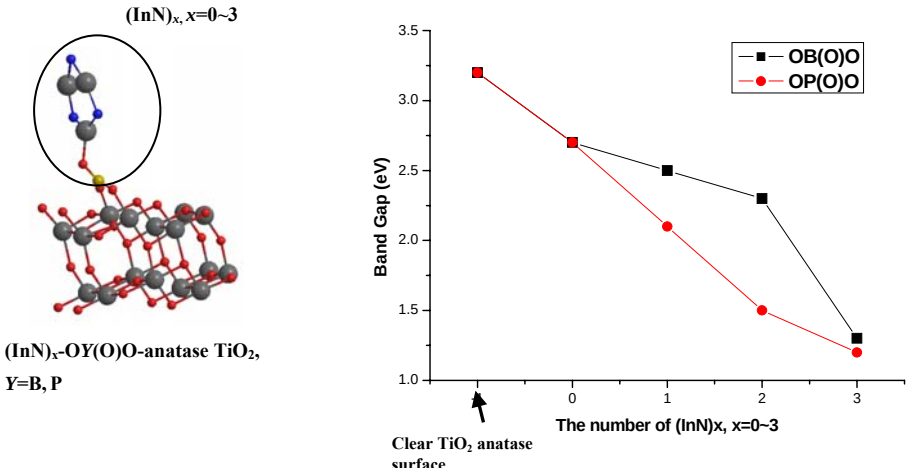

Figure 1. Predicted band gaps of $(InN)_x$-OY(O)O-TiO_2 anatase

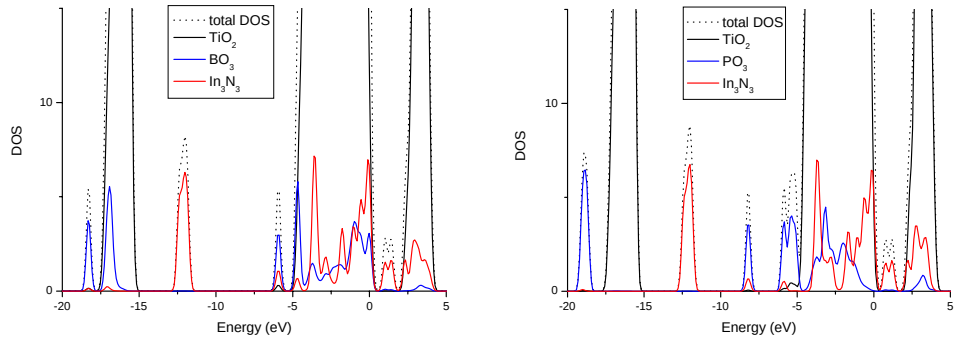

Figure 2. Predicted densities of states of $(InN)_3$ - OY(O)O - TiO_2 anatase with Y=B and P.

Besides, the Bader charge analyses show that more electron density is transferred from TiO_2 to the –OB(O)O– linker, than to the –OP(O)O– linker.

In conclusion, based on the above result, we can conclude that the –OB(O)O– is an efficient chemical bond to link InN and TiO_2. More discussion on the –OP(O)O– linker is given below.

(二) J. S. Lin（林志興）：

To establish better understanding of the significant different effect of different anchoring groups, i.e. H_3PO_3 vs H_3BO_3, on the solar energy conversion of InN/TiO_2 solar cell design[1] we began to investigate the different stable structural modes of InN-XO_3^{2-} (X=B and P) adsorbed on both TiO_2 anatase (101) and TiO_2 rutile (110) surfaces and their corresponding electronic properties to rationalize the main reasons to cause the significant different effect of different anchoring groups on the photoexcitation within the UV/Vis region and the electron injection from the photoexcited electronic states to the unoccupied electronic states around the

lowest conduction bands of InN-XO_3^{2-} (X=B and P) adsorbed on both TiO_2 anatase (101) and TiO_2 rutile (110)surfaces.

We first calculated the structural models of dissociated H_3PO_3, i.e. $H_3PO_3 \rightarrow 2H^+ + HPO_3^{2-}$, adsorbed on both TiO_2 anatase (101) and TiO_2 rutile (110) surfaces. Our calculated results indicated that the most stable structural mode of both $2H^+$ and HPO_3^{2-} adsorbed on TiO_2 anatase (101) surface is through 1) the bonding between surface 5-fold coordinated of Ti, i.e. $Ti_{cn5,}$ and two oxygens within adsorbed HPO_3^{2-} 2) the bonding between the adsorbed $2H^+$ and surface 2-fold coordinated O, i.e. $O_{cn2.,}$ and 3) the very weak bonding between the third oxygen within adsorbed HPO_3^{2-} and adsorbed $2H^+$, that is $-(O_{cn2})_2-(H)_2-OHP(O)_2-(Ti_{cn2})_2-$. However, we found that the most stable structural mode of dissociated H_3PO_3 adsorbed on TiO_2 rutile (110) surface is through 1) the bonding between surface Ti_{cn5} and two oxygens within adsorbed HPO_3^{2-} and 2) the bonding between the adsorbed $2H^+$ and surface $O_{cn2,}$ that is, $-(O_{cn2})_2(H)_2POH(O)_2-(Ti_{cn2})_{2.}$ These two structural models are shown below, respectively.

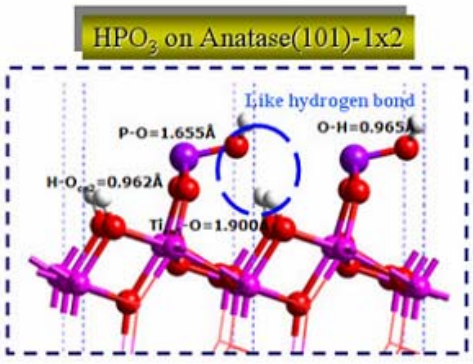

Eads=1.44Ev

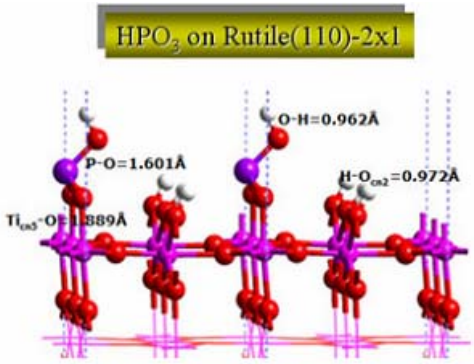

Eads=1.27eV

We then move on to investigate the electronic properties of these two structural models in order to establish the energy diagram to qualitatively rationalize both photoexcitation and electron injection process for possible interfacial electron transfer between adsorbed HPO_3^{2-} and TiO_2 surfaces.[2] To elaborate this in detail, we calculate the PDOS for adsorbed HPO_3^{2-} and that for both surface and bulk layer for the TiO_2 surfaces as shown in the figure below.

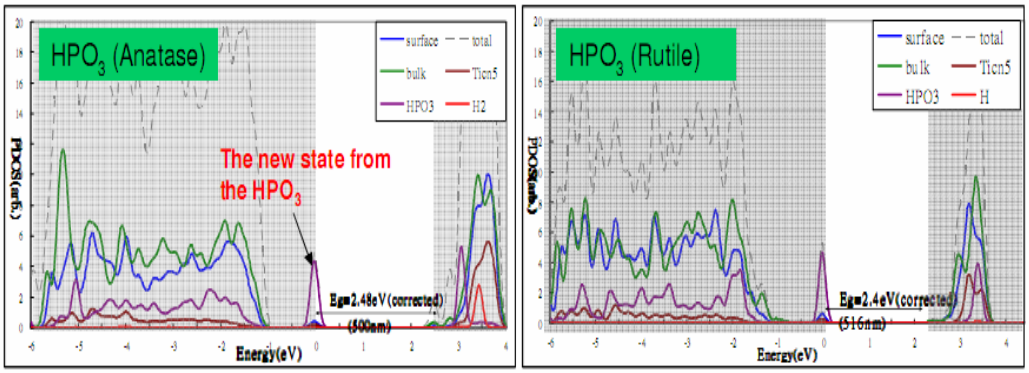

As you will see from the Fig. on the left above the adsorbed HPO_3^{2-} will cause the appearance of the new occupied electronic states between the band gaps arisen from the clear TiO_2 anatase (101) surface. Apparently, the adsorbed HPO_3^{2-} will cause the reduction of the band gap from 3.2 eV to 2.48 eV to provide the possibility of photoexcitation at the 2.48 eV (~500 nm) within the UV/Vis adsorption region. However, if we compare our calculated PDOS of the TiO_2 anatase (101) surface layer with those of adsorbed HPO_3^{2-} we immediately found that there are no suitable energy matches between those lower unoccupied electronic states of adsorbed HPO_3^{2-} and the unoccupied electronic states around those lower conduction band edges of the TiO_2 anatase (101)

surface and bulk layers. As regard to the structural model of HPO_3^{2-} adsorbed on TiO_2 rutile (110) surface we again found the appearance of the new occupied electronic states between the band gaps arisen from the clear TiO_2 rutile (110) surface. Apparently, the adsorbed HPO_3^{2-} will cause the reduction of the band gap from 3.0 eV to 2.4 eV to provide the possibility of photoexcitation at the 2.40 eV (~516 nm) within the UV/Vis adsorption region. Additionally, there are no suitable energy matches between the lower unoccupied electronic states of adsorbed HPO_3^{2-} and the unoccupied electronic states around the lower conduction band edges of the TiO_2 rutile (110) surface and bulk layers. In summary, our both structural models of HPO_3^{2-} adsorbed on both TiO_2 anatase (101) and TiO_2 rutile (110) surfaces will possibly provide the sensible structural modes for being used to effectively convert light into the photoexcited states of adsorbed InN on both TiO_2 anatase (101) and TiO_2 rutile (110) surfaces but unlikely provide a feasible interfacial electron pathway for electron injection through the HPO_3^{2-}/TiO_2 interface.

We then further calculated the different structural modes of InN adsorbed on both H_3PO_3 anchored TiO_2 anatase (101) and rutile (110) surfaces leading to InN-PO_3^{2-} adsorbed onto both TiO_2 anatase (101) and rutile (110) surfaces to see the effect of this anchoring group, i.e. H_3PO_3, on both photoexcitation and electron injection processes involved for converting light into the electricity in the InN/TiO_2 sensitized solar cell system. The following structural modes of InN-PO_3^{2-} adsorbed on TiO_2 anatase (101) surface as shown below are calculated. The most stable

structural mode is the InN-PO_3^{2-} side-on adsorption structure, i.e. -O_3P-NIn-OPO_2-, through the bonding between In within InN and O within PO_3^{2-}.

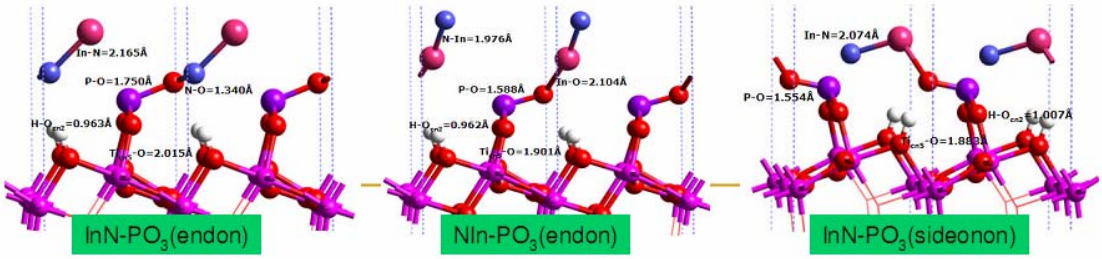

Regarding to the structural modes of InN-PO_3^{2-} adsorbed on TiO_2 rutile (110) surface the following structural modes as shown below are investigated. The most stable structural mode is the end-on structure of adsorbed InN-PO_3^{2-} on TiO_2 rutile (110) surface as shown on the left below.

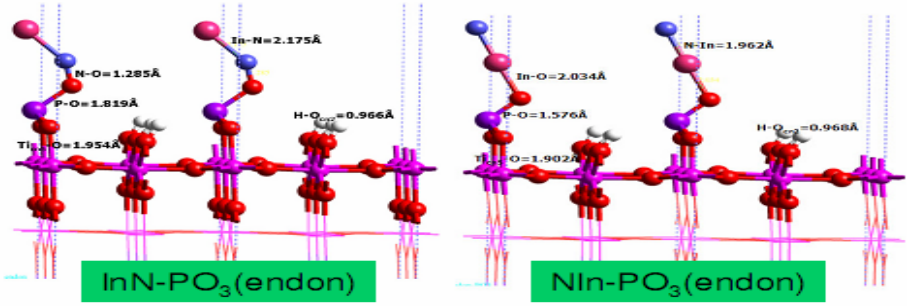

Now we investigate the electronic properties of the most stable structural mode of InN-PO_3^{2-} adsorbed on the TiO_2 anatase (101) surface, i.e. the side-on structure of InN-PO_3^{2-} adsorbed on the TiO_2 anatase (101) surface, as shown below. From our calculated PDOS of adsorbed InN-PO_3^{2-} we can observe the appearance of the new states due to the adsorption of InN-PO_3^{2-} within the bandgap originated from the clean TiO_2 anatase (101) surface to cause the reduction of the bandgap from 3.2 eV to 2.02

eV to provide the possibility of photoexcitation at the 2.02eV (~613 nm) within the UV/Vis adsorption region. However, there are no corresponding unoccupied electronic states due to the adsorbed InN-PO_3^{2} around the conduction band edge. Therefore, by comparing the PDOS of adsorbed InN-PO_3^{2} with that of TiO_2 anatase (101) surface and bulk layers we found there are no suitable energies match to provide the feasible interfacial electron pathway for electron injection through the interface between InN-PO_3^{2-} and TiO_2 anatase (101) surface.

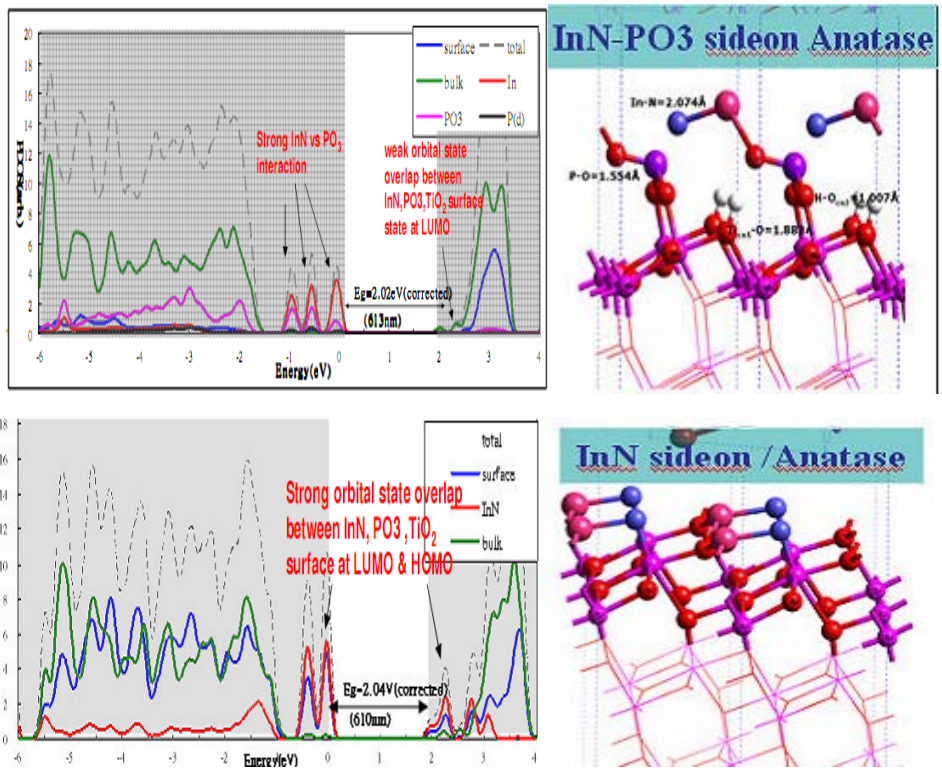

In addition, we compare the electronic properties of the most stable structural mode of InN adsorbed (side-on) on the TiO_2 (101) anatase surface with that of the most stable structural mode of InN-PO_3^{2-} adsorbed (side-on) on the TiO_2 anatase (101) surface as shown above in order to understand the effect of the anchoring group, i.e. H_3PO_3, on the electronic states governing the variation

of the bandgap and the extent of overlap of the unoccupied electronic states around the band edges of the conduction bands between the adsorbate, i.e. adsorbed InN and adsorbed InN-PO_3^{2-}, and the TiO_2 surfaces. We first found that both stable structural modes of InN adsorbed (side-on) on TiO_2 anatase (101) surface and InN-PO_3^{2-} adsorbed (side-on) on TiO_2 anatase (101) surface have very similar bandgaps: 2.04 eV vs 2.02 eV. It indicates that both structural modes provide very similar photoexcitation at the 2.40 eV (~516 nm) within the UV/Vis adsorption region. We also found that both structural modes of InN adsorbed (side-on) on TiO_2 anatase (101) surface and InN-PO_3^{2-} adsorbed (side-on) on TiO_2 anatase (101) surface have quite different distributions of unoccupied electronic states around the conduction band edges. For the InN adsorbed (side-on) on TiO_2 anatase (101) surface the unoccupied electronic states around the conduction band edges have a very strong overlap among adsorbed InN, TiO_2 anatase (101) surface and TiO_2 anatase (101) bulk. Consequently, as soon as the photoexcitation proceeds, this photoexcited electron will be easily injected into the TiO_2 anatase (101) surface. It was then further leaded to the TiO_2 anatase (101) bulk to effectively and rapidly transfer the photoinduced electrons. But for the InN-PO_3^{2-} adsorbed (side-on) on TiO_2 anatase (101) surface there are negligible overlap of the unoccupied electronic states around the conduction band edges among the adsorbed InN-PO_3^{2-}, TiO_2 anatase (101) surface and TiO_2 anatase (101) bulk. Therefore, the photoexcited electron will not be injected into the TiO_2 anatase (101) surface leading to TiO_2 anatase (101) bulk.

Main discoveries and Conclusions

To elaborate the different electronic properties between InN adsorbed (side-on) on TiO_2 anatase (101) surface and InN-PO_3^{2-} adsorbed (side-on) on TiO_2 anatase (101) surface we further analyze the electronic density of InN adsorbed (side-on) on TiO_2 anatase (101) surface and InN- PO_3^{2-} adsorbed on TiO_2 anatase (101) surface. Based on our calculated electron density of the lower conduction bands of InN adsorbed (side-on) on TiO_2 anatase (101) surface as shown below we found that there is a strong overlap between the π characteristic from adsorbed InN and that from Ti_{cn5}. to give rise to the effective channel for electron injection from adsorbed InN to TiO_2 anatase (101) surface. However, this kind of overlap between PO_3^{2-} and Ti_{cn5} doesn't occur to the InN-PO_3^{2-} adsorbed (side-on) on TiO_2 anatase (101) surface. Rather than there is a strong overlap between the σ characteristic from adsorbed InN and that from PO_3^{2-}. Consequently, this system will not provide the feasible channel for electron injection through the InN-PO_3^{2-} to TiO_2 anatase (101) surface. Therefore, the significant different bonding nature within the interface of both InN adsorbed (side-on) on TiO_2 anatase (101) surface and InN-PO_3^{2-} adsorbed (side-on) on TiO_2 anatase (101) surface, i.e. π characteristic vs σ characteristic, is the main reason for causing the significant different solar energy conversion.

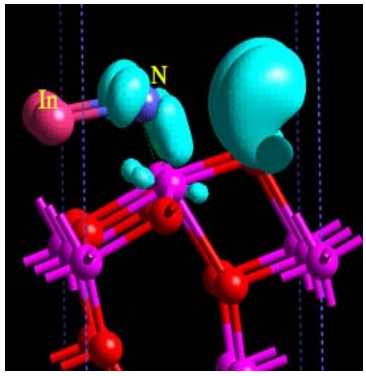

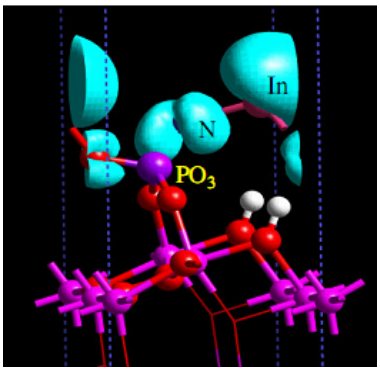

We are presently investigating the effect of different anchoring group, i.e. H_3BO_3, on the photoexcitation of InN adsorbed onto TiO_2 surface within the UV/Vis region and the electron injection from the photoexcited electronic states to the unoccupied electronic states around the conduction band edges of the TiO_2 surfaces. By comparing the effects of these two anchoring groups on the electronic properties of InN adsorbed on TiO_2 surfaces we hope that we will provide much better understanding into the reason why the anchoring group, i.e. H_3BO_3, will cause the significant enhancement of solar energy conversion through the InN-BO_3^{2-}/TiO_2 interface.

References:

1. J.-H. Wang and M. C. Lin, ChemPhysChem, 2004, 5, 1615.
2. J. S. Lin, W.-C. Chou, S.-Y. Lu, G.-J. Jang, B.-R. Tseng and Y.-T. Li, J. Phys. Chem. B, 2006, 110 23460-23466

四、Functionalization of TiO_2 surface (P. Raghunath, W. F. Huang and M. C. Lin):

Adsorption Configurations and Reactions of Boric Acid on TiO_2 Anatase (101) Surface

This study investigates the adsorption and reactions of the monomer and dimer of $B(OH)_3$ on TiO_2 anatase (101) surface by first-principles calculations based on the density functional theory and pseudopotential method. On the clean surface, the most stable adsorption structure for $B(OH)_3$ is a molecular monodentate configuration with one hydrogen bonded to a neighboring surface bridging oxygen; its adsorption energy is 17.2 kcal/mol. The bidentate bridging configuration with two O atoms of the OH groups of boric acid binding to two 5-fold-coordinated Ti atoms has an adsorption energy of 13.5 kcal/mol. The adsorbed $B(OH)_3$ molecule can dissociate into the bidentate adsorption configuration, Ti-OB(OH)O-Ti(a), in which the -OB(OH)O- moiety binds to the surface through two Ti-O bonds with two H atoms on bridged surface oxygen atoms, following two successive H-migrates with barriers of 8.4 and 15.2 kcal/mol. The overall exothermicity is 10.8 kcal/mol. Significantly, the adsorption energy for Ti-OB(OH)O-Ti(a) with 2 H on two O_{2c} surface atoms is 140.1 kcal/mol. Another pathway for H_2O elimination from $B(OH)_3$ on the surface requires an energy barrier of 37.3 kcal/mol. In the case of dimer there are two identical molecules like the monodentate configuration of $B(OH)_3$ adsorbed on two 5-fold-coordinated Ti atoms of the surface with an adsorption energy of 34.2 kcal/mol. The Ti–OB(OH)OB(OH)O-Ti binding with 2 H on two O_{2c} surface atoms is very strong like the monomer case; its adsorption energy is 150.0 kcal/mol. Thus both Ti-OB(OH)O-Ti and Ti-OB(OH)OB(OH)O-Ti adsorbates can be employed as strong linkers between semiconductor quantum dots such as InN and

TiO_2 nanoparticles. The mechanisms of these surface reactions have also been explicitly elucidated with the computed potential energy surfaces. Most of the $B(OH)_3$ reactions on the anatase surface are exothermic. This Work will be communicated to J. Phys. Chem. C.

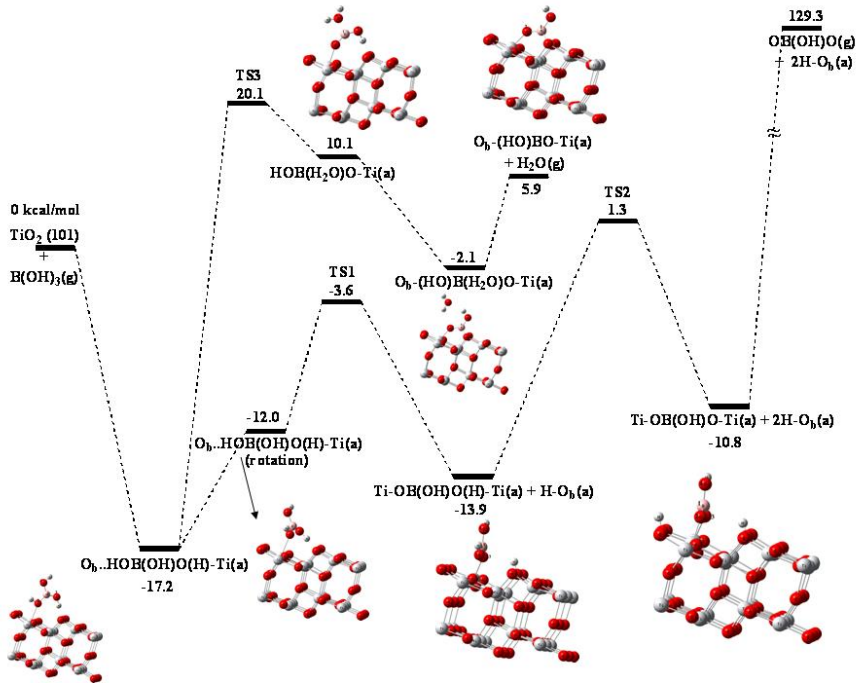

Figure 1. Potential energy surface of the surface reactions starting with *cis* conformation of $B(OH)_3(g)$ on TiO_2 anatase (101) surface.

Adsorption Configurations and Reactions of Boric Acid on TiO_2 Rutile (110) Surface

In this work, we have systematically studied the monomer and dimer of boric acid molecules adsorption and reactions on rutile TiO_2 (110) surface using first-principles calculations. The most stable adsorption structure for $B(OH)_3$ on the clean surface is a molecular monodentate configuration with one hydrogen bonded to a neighboring surface bridging oxygen; its adsorption energy is

19.4 kcal/mol. The resulting O_b..HOB(OH)O(H)-Ti(a) complex is predicted to have large adsorption energies and is possible to overcome the barriers for H atoms to migrate to neighboring bridged oxygens producing stable Ti-OB(OH)O-Ti(a) + 2H-O_b(a) with an estimated exothermicity of 23.7 kcal/mol. Another product is the elimination of H_2O from this intermediate with a high energy barrier (37.9 kcal/mol) giving rise to the O_b-B(OH)O-Ti(a) adsorbate which is endothermic by 7.6 kcal/mol.

A similar study on the reactions of 2 $B(OH)_3$ on the surface produces the two identical molecules like monodentate configurations of $B(OH)_3$ adsorbed on two 5-fold-coordinated Ti atoms of the anatase surface with an adsorption energy of 37.9 kcal/mol, which is almost 2 times that of the monodentate, reflecting a negligible adsorbate-adsorbate interaction because of the planar $B(OH)_3$ structure. Elimination of H_2O from the 2(Ob..HOB(OH)O(H)-Ti(a)) complex required 38.8 kcal/mol of energy. To further decompose into Ti-OB(OH)OB(OH)O-Ti(a) and 2H-O_b(a) is predicted to be exothermic by 21.0 kcal/mol. For the intermediate Ti-O(H)B(OH)OB(OH)O(H)-Ti(a) the required activation energy for H- migration from the bonding O-H groups is 4.4 kcal/mol for the first O-H breaking and 3.1 kcal/mol for the second O-H breaking. We found that dissociation reaction processes of boric acid on the rutile surface are energetically more favorable than anatase surface. The final products of boric acid dissociative adsorptions Ti-OB(OH)O-Ti and Ti–OB(OH)OB(OH)O-Ti bond very strongly with TiO_2 anatase surface respectively with 134.6 and 141.2 kcal/ml binding energies

when H atoms are co-adsorbed on their neighboring bridged surface O atoms. These species may be quite useful for interface linking between the semiconductor quantum dots such as InN and TiO_2 nanoparticles in the fabrication of solar cells.(This Work will be communicated to J. Phys. Chem. C)

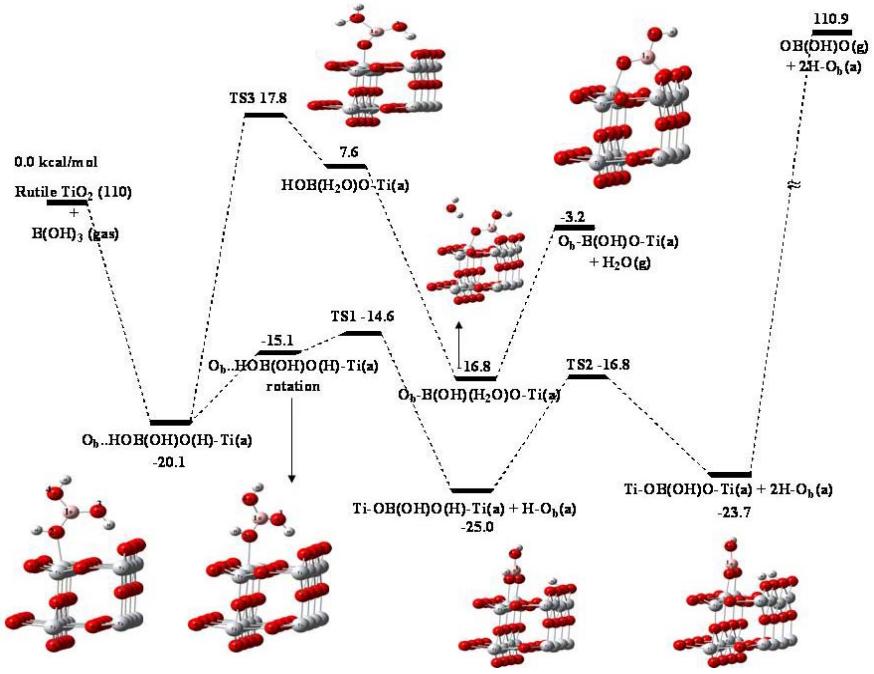

Figure 2**:** Potential energy surface of the surface reactions starting with *cis* conformation of $B(OH)_3$(g) on TiO_2 Rutile (110) surface.

Adsorption and Reaction of H_2O_2 and H_2S on clean TiO_2 Anatase (101) and TiO_2-Rutile (110) Surface by First - Principles Calculations

This study investigates the adsorption and reaction of hydrogen peroxide (H_2O_2) and hydrogen sulfide (H_2S) on the clean anatase TiO_2 (101) and rutile TiO_2 (110) surfaces by first-principles calculations based on the density functional theory (DFT) with generalized gradient approximation (GGA) and the

pseudopotential method with 500-eV plane-wave expansion. The slab model is adopted to calculate the interaction between the TiO_2 solid phase and gas phase molecule. It includes 18 and 12 [TiO_2] primitive cells with a 13.521 Å vacuum space for H_2O_2 and H_2S above the TiO_2-anatase surface respectively, and the corresponding values on TiO_2-rutile are 24 and 16 [TiO_2] primitive cells with 13.172 for H_2O_2 and H_2S above the TiO_2-rutile surface respectively. There are four different adsorption sites on the surface; they are five-fold coordinated titanium, six-fold coordinated titanium, two-fold bridging oxygen, and tree-fold coordinated oxygen, corresponding to Ti_{5c}, $Ti_{6c,}$, O_{2c}, and O_{3c}, respectively.

The results of H_2O_2 on clean TiO_2 surface

As shown in Figure 3, the potential energy surface and the adsorption energy for the reaction of H_2O_2 with TiO_2 have been constructed. It was found that H_2O_2 and its fragments, HO, H_2O and O, adsorb on the -Ti_{5c} and (-Ti_{5c})$_2$ site with large adsorption energy, from 18.6 kcal/mol to 73.6 kcal/mol. The similar adsorption structures on TiO_2-rutile and on TiO_2-anatase surface have close adsorption energies. According to our calculation, the barriers of H_2O_2 decomposition to two HO radicals are 31.3 kcal/mol and 22.5 kcal/mol on TiO_2-anatase and TiO_2-rutile surface respectively. The formation of surface oxygen species by H_2O decomposition on the TiO_2 surface with an exothermicity of 3.5 kcal/mol and 2.7 kcal/mol on TiO_2-anatase and TiO_2-rutile surface respectively. (This calculation will be published on JPCC.)

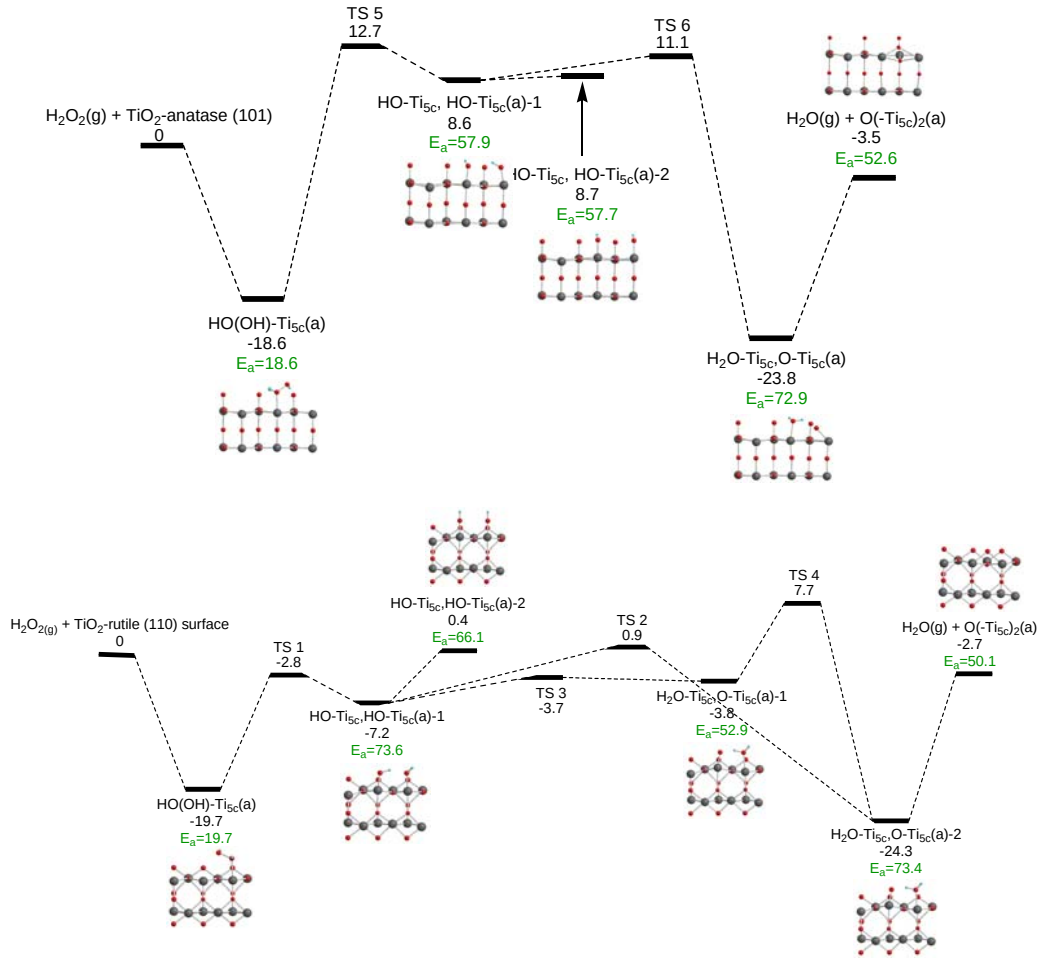

Figure 3. Schematic potential energy surfaces for the reaction H_2O_2+TiO_2. (only helf depth of the TiO_2 surface model)

The results of H_2S on clean TiO_2 surface

As shown in Figure 4, the potential energy surface and the adsorption energy for the reaction of H_2S with TiO_2 have been constructed. It was found that H_2S and its fragments, HS, H and S, adsorb on the -Ti_{5c}, -O_{2c}, (-Ti_{5c})$_2$, and v-O_{2c} site with large adsorption energy, from 11.4 kcal/mol to 188.4 kcal/mol. Here v-O_{2c} expresses vacancy site of O_{2c}. The barriers of the H_2S dehydrogenation processes producing SH + H and S + 2H are 6.2 and 13.1 kcal/mol on TiO_2-anatase, respectively. The

corresponding barriers on TiO_2-rutile surface are 3.1 and 30.6 kcal/mol. The formation of surface sulfur species by a complete O↔S exchange at the surface with an endothermicity of 5.0 kcal/mol on TiO_2-anatase and 15.4 kcal/mol on TiO_2-rutile may be the most likely reaction mechanism. (This calculation will be published on JPCC.)

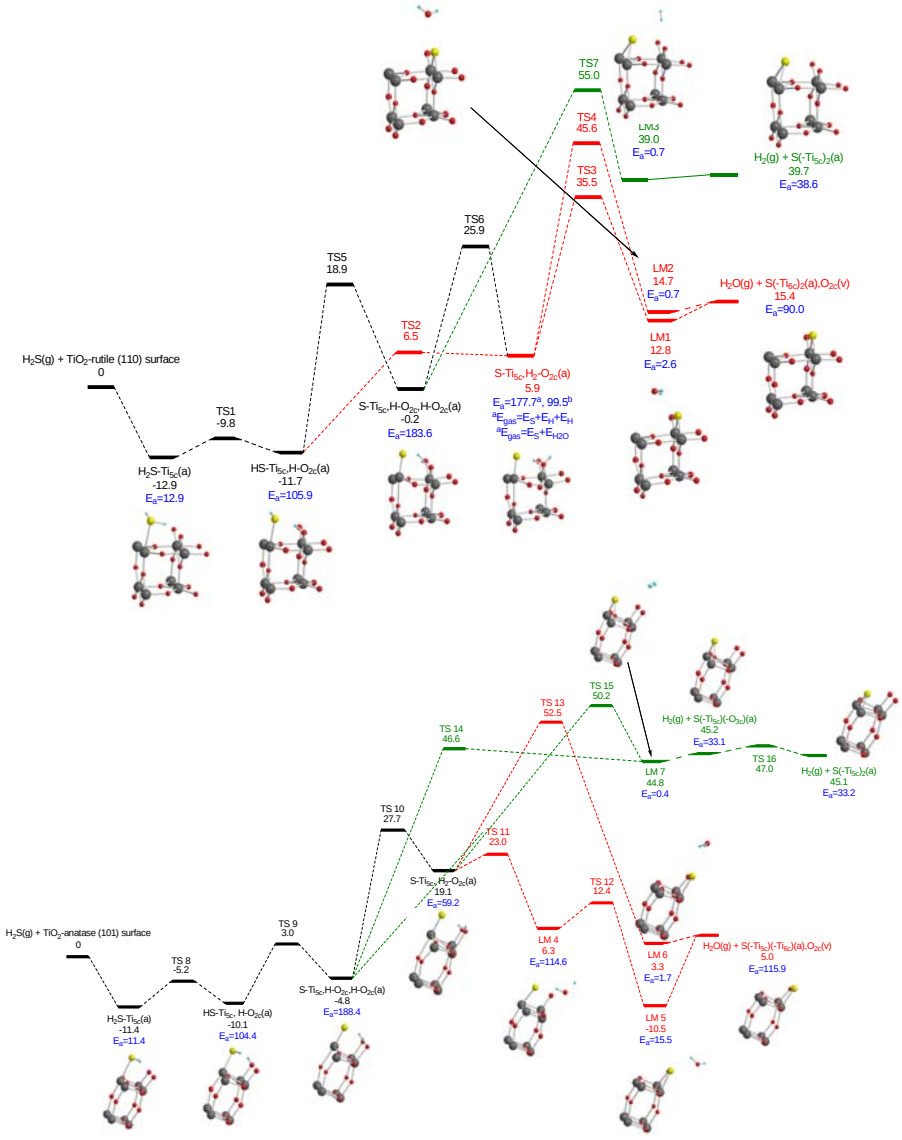

Figure 4. Schematic potential energy surfaces for the reaction H_2S + TiO_2. (only half depth of the TiO_2 surface model)

五、Relativistic parameterization of the SCC-DFTB method（Henryk Witek):

Techniques allowing quantum chemical calculations for large molecular systems are the subject of intensive research and development in recent years. One of the most promising methods belonging to this category is the self-consistent charge density-functional tight-binding (SCC-DFTB) method.[1,2] It is a semiempirical computational technique that allows for fast and rather reliable determination of molecular structures, energetics, and vibrational spectra of medium and large-size molecular systems. Only valence electrons are considered explicitly in SCC-DFTB. Therefore, this method allows substantially larger number of atoms to be included in the system under investigation than traditional ab initio methods. The price to be paid for noticeably higher performance of SCC-DFTB in comparison with standard quantum chemical methodologies (e.g., BLYP/cc-pVDZ or B3LYP/cc-pVDZ) is somewhat lower accuracy of this method; at the same time the computational effort is reduced substantially even by a few orders of magnitude. SCC-DFTB and other related approaches, like DFTB[3] and spin-polarized SCC-DFTB[2], have been applied over the last two decades for simulations of various chemical and physical properties of large number of molecules and materials, e.g., to investigate the infrared and Raman spectra of various carbon nanomaterials,[4,5] starting from fullerenes and ranging up to assemblies of fullerenes and nanotubes.[6]

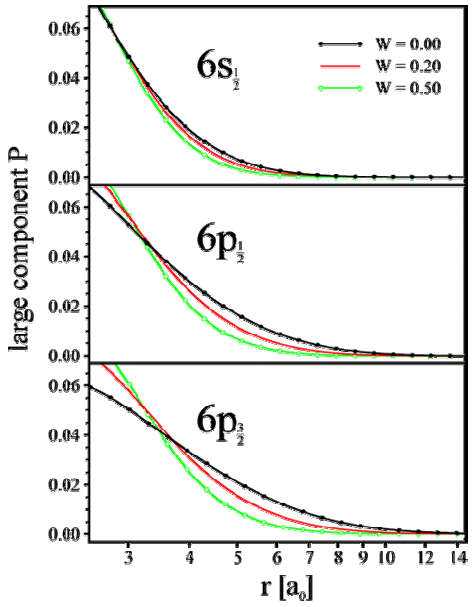

Figure 1. Contraction of the large component radial function P of the $6s_{1/2}$, $6p_{1/2}$, and $6p_{3/2}$ spinors of lead in the valence region. The wave functions have been calculated with three different values of W (W = 0.00, 0.20, and 0.50) defining the confining Woods-Saxon potential.

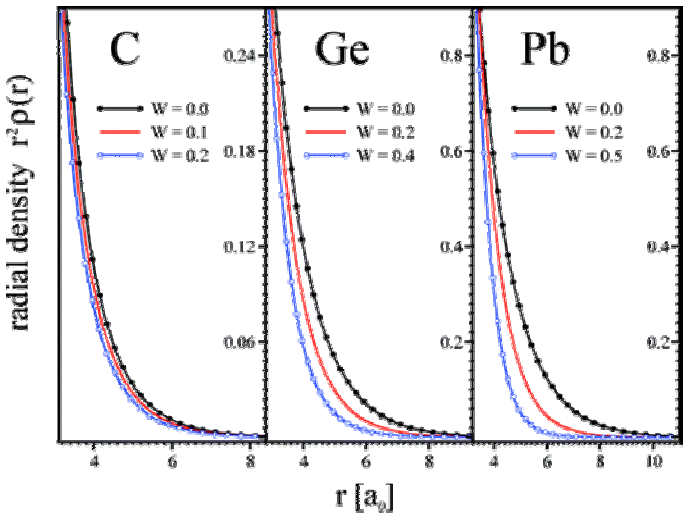

Figure 2.

Contraction of the radial electron density of carbon, germanium, and lead in the valence region. The densities have been calculated with three different values of W defining the confining Woods-Saxon potential.

In the present report, we discuss our accomplishments in developing a consistent set of Slater-Koster files for the self-consistent charge density-functional tight-binding method.

The SCC-DFTB method, unlike most of quantum chemical methods, does not use sensu stricto the concept of basis set. Instead, so called Slater-Koster files are employed that contain analogous portion of information. The main advantage of using these files - that contain all needed molecular integrals computed at all feasible distances - is the possibility of skipping the overlap and Hamiltonian integrals determination in the SCC-DFTB calculations, what speeds up the computational process appreciably. One of the largest practical drawbacks of SCC-DFTB is its limited applicability stemming from incomplete set of the parameter files. The existing parameterization of the SCC-DFTB method is limited to only five elements: carbon, hydrogen, nitrogen, oxygen, and sulfur. For these elements, there exist a unified set of Slater-Koster files that has been extensively tested.[7,8,9] There also exists a number of scattered Slater-Koster files for other pairs of elements (including gallium, boron, zinc, iron, copper, and a few others) that have been developed independently from the CNOHS set and cannot be used simultaneously in one calculation owing to the lack of correspondence of employed atomic radii and confinement potentials. The relativistic parameterization of SCC-DFTB that we discuss in this report allows a unified set of Slater-Koster files to be developed for all possible pairs of chemical elements. Such a parameterization could not be developed with the existing parameterization program due to three reasons: i) no *f* orbitals could be used in the old parameterization program; ii) the accuracy of calculated integrals did not permit accurate deductions of their

second derivatives; iii) no relativistic effects were included in the old parameterization program. The new parameterization program reported here allows for overcoming these difficulties and consequently, for producing an extended set of Slater-Koster files.

Main discoveries and conclusions

A number of intermediate stages can be identified in the process of relativistic parameterization of the SCC-DFTB method. The initial stage concerns solving atomic DFT problem to produce atomic densities, atomic exchange-correlation potentials, and a set of valence Kohn-Sham orbitals. This step requires solving numerically the radial atomic Kohn-Sham problem. To incorporate the relativity in the formalism, we have chosen to solve a four component Dirac-Kohn-Sham problem. In relativistic regime, the radial equation can be reduced to a set of coupled differential equations for the *f* and *g* radial wave functions. A solution to this problem is sought following Desclaux.[10] We have adopted the classical program of Desclaux, in which the standard LDA and PBE exchange-correlation potentials replaced the original $X\alpha$ potential of Slater. This approach gives us many benefits since it allows for accurate generation of atomic densities and orbitals without usual finite basis set limitations. The algorithm for numerical integration of the atomic Dirac-Kohn-Sham equations, needed as an initial step for the parametrization of the self-consistent-charge density-functional tight-binding method, has been described in details in the first of the resulting publications [J. Phys. Chem. A, 2007, 111, 5712] together with

initial tests of the presented approach. The required one-component quantities, i.e., orbital energies, orbital wave functions, and Hubbard parameters, are obtained by weighted averaging of the corresponding numbers determined for the atomic spinors. The wave function and density confinement is achieved by introducing the Woods-Saxon potential in the atomic four-component Dirac-Kohn-Sham problem. The effect of the additional confining potential on energy eigenvalues and the shape of atomic wave functions and densities is discussed and numerical examples are presented for the valence spinors of carbon, germanium, and lead.

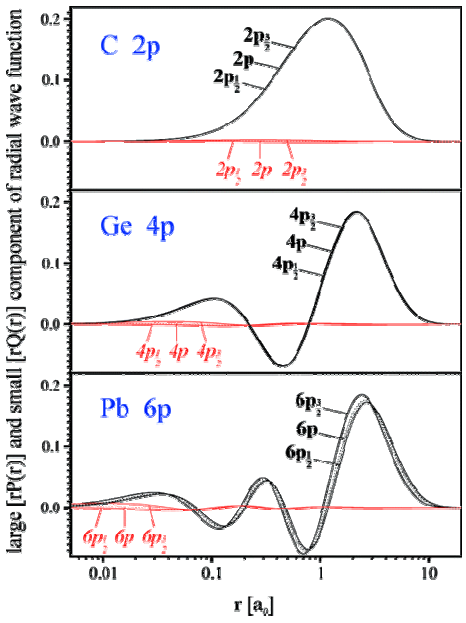

Figure 3. Plots of large (bold characters) and small (slant characters) components of the atomic spinor (solid line) and orbital (dotted line) radial wave functions for the 2p shell of carbon, the 4p shell of germanium, and the 6p shell of lead.

Next stage of the parameterization process concerns writing a program to calculate two-center Hamiltonian and overlap integrals. The distance-dependent integrals are calculated using previously

determined atomic orbitals and corresponding atomic densities. We have employed a two-dimensional numerical Gauss-Legendre quadrature in modified prolate spheroidal coordinates. The modification has been introduced to allow for better distribution of the quadrature points.[11] All possible types of integrals - overlap, kinetic energy, and over the effective potential - have been shown to reduce to two classes of integrations that can be both performed with our numerical integration program. A substantial effort has been done to test the integration routine to ensure correct numerical results. After such extensive tests, we are confident that the integration yields correct numerical values. The integration program has been subsequently wrapped in a shell script to allow automatic determination of the electronic part of the Slater-Koster files. The resultant script has been tested for reproducing the existing set of Slater-Koster files for carbon and hydrogen. At present, we have succeeded to reproduce the electronic part of the existing CNOHS backbone set of Slater-Koster files. The set has been extended to further elements, fluorine, chlorine and boron. Unfortunately, for the extended elements, we have not been able yet to perform the optimization of the confining radii that assure proper numerical accuracy of the SCC-DFTB method for molecules containing these elements. We are currently working on these topics. The present research effort concerns also computing repulsive, two-center SCC-DFTB potentials. Usually, such potentials are obtained from auxiliary DFT calculations performed for a chosen group of chemicals over a broad range of distances. We have shown that this scheme not necessarily leads to best

agreement with experimental findings. An alternative scheme has been proposed, where the repulsive potentials are obtained directly from experimental data. We showed that this new scheme can reproduce the geometrical and vibrational parameters with better accuracy than corresponding DFT results.[12] Considerable effort has been devoted to finding a well-defined procedure of developing the repulsive potential through a fit to experimental data on energetics, geometries, and vibrational frequencies of a wide class of molecules. At present, the most promising approach seems to be a genetic algorithm scheme, where an initial starting potentials is optimized using a series of mutations and crossovers to fit maximally the available experimental data. For elements where no sufficient data are available, an alternative approach can be used where the repulsive potentials are fitted to the results of accurate quantum chemical calculations employing either multireference CI or multireference perturbation theory. We hope to conclude this research soon and present the final results in a series of publications.

The most involved part of the parameterization process devoted to developing a set of parameterization computer programs is almost completed. From now on, we are focusing our main research effort on using the developed machinery to produce Slater-Koster files that are of interest for the INER group. To this end, at our last INER presentation, we have urged other participating research groups to send to us a list of elements that would allow for faster and more robust calculations for their systems of interest. We are planning to successively develop

Slater-Koster files for those elements in the first place. We hope that the developed files can be used to speed up their theoretical simulations.

References:

1. M. Elstner, D. Porezag,G. Jungnickel, J. Elsner, M. Haugk, T. Frauenheim, S. Suhai and G. Seifert, Phys. Rev. B, 1998, 58, 7260
2. C. Köhler, G. Seifert, U. Gerstmann, M. Elstner, H. Overhof and T. Frauenheim, Phys. Chem. Chem. Phys., 2001, 3, 5109
3. D. Porezag, T. Frauenheim, T. Köhler, G. Seifert and R. Kaschner, Phys. Rev. B, 1995, 51, 12947-12957
4. H. Witek, K. Morokuma and A. Stradomska, J. Chem. Phys., 2004, 121, 5171
5. H. A. Witek, S. Irle, G. Zheng, B. de Jong and K. Morokuma, J. Chem. Phys., 2006, 125, 214706
6. H. A. Witek, B. Trzaskowski, E. Malolepsza, K. Morokuma and L. Adamowicz, Chem. Phys. Lett., 2007, 446, 87
7. T. Krüger, M. Elstner, P. Schiffels and T. Frauenheim, J. Chem. Phys., 2005, 122, 114110
8. H. A. Witek and K. Morokuma, J. Comp. Chem., 2004, 25, 1858
9. K. W. Sattelmeyer, J. Tirado-Rives and W. L. Jorgensen, J. Phys. Chem. A, 2006, 110, 13551
10. J. Desclaux, Comp. Phys. Comm.**,** 1969, 1, 216
11. A. D. Becke, J. Chem. Phys.**,** 1982, 76, 6037
12. E. Malolepsza, H. Witek and K. Morokuma, Chem. Phys. Lett., 2005, 412, 237

六、Ethanol to H_2 conversion（C. S. Lee and M. C. Lin):

The goals of this project are to prepare and characterize new catalysts to produce hydrogen from ethanol reforming reaction for fuel cell applications. This report covers the time period of January 1, - December 31, 2007. Sevaral catalysts have been prepared and tested include 1) Ru/Al_2O_3, 2) $Rh/Ce_xZr_{1-x}O_2$, 3) Pt_xRu_{1-x}, 4) Pt_xRu_{1-x}/CeO_2, as well as commercial three ways catalysts. During this year four conference posters were presented.[1-4]

Ethanol is attractive to be a fuel for hydrogen production because of its relatively high hydrogen content, availability, non-toxicity and facile storage and handling safety. For hydrogen to be used in fuel cell system, one of the methods suggested for processing bio-ethanol to produce H_2 is catalytic steam reforming reaction. In biomass fuel cell application, ethanol could be catalyzed and undergoing autothermal reaction by noble metal catalyst in the presence of water. The catalytic process could be shown as following three reactions:

$C_2H_5OH+3O_2 \rightarrow 3H_2O+2CO_2$ $\Delta H_R \fallingdotseq$ -1280KJ/mol (oxidation reaction) ------(1)

$C_2H_5OH+1/2O_2 \rightarrow 2CO+3H_2$ $\Delta H_R \fallingdotseq$ +20KJ/mol (partial oxidation reaction) ------(2)

$CO+H_2O \rightarrow CO_2+H_2$ $\Delta H_R \fallingdotseq$ -40KJ/mol (Water-Gas shift reaction) ------(3)

It shows that five moles hydrogen per one mole of ethanol can be produced and the optimized selectivity of hydrogen is 166%. In recent years, it has attracted many research groups around the world to develop new catalysts for ethanol reforming

reaction. Among many catalysts, the Rh/CeO_2 catalyst exhibits an excellent selectivity for hydrogen and excellent stability for the steam reforming of ethanol.[5]

Our previous study on the morphology control of CeO_2 nanocrystals indicates that the catalytic properties of a Rh-ceria catalyst is greatly influenced by the nature of the exposed surface on CeO_2 nanocrystals.[6] This shape-dependent property provides an efficient means to investigate other catalysts consisting of metal oxides of controlled size and shape. Both rod and cubic samples showed initially a rate of conversion of H_2 greater than for an irregular CeO_2 catalyst, but their activity gradually decreased because of an altered CeO_2 morphology. A possible way to maintain the stability of CeO_2 nanocrystals is to dope a stable metal, such as Ti or Zr.

In this report, the research extended previous results in characterizing the catalyst and operating parameters. We compared the autothermal ethanol reforming reaction on several catalysts include: 1) Ru/Al_2O_3, 2) $Rh/Ce_xZr_{1-x}O_2$, 3) Pt_xRu_{1-x}, 4) Pt_xRu_{1-x}/CeO_2, as well as commercial three ways catalysts.

Experimental

1. Catalysts[7-13]:

(1) Ru/Al_2O_3: A catalyst with irregular Ru particles was first prepared on impregnating alumina support (Al_2O_3, 300 m^2/g, average diameter 1.2 mm) with an aqueous solution of $RuCl_3 \bullet 2H_2O$ (99.9%, STREM), followed by oven drying at 120 °C for 6 h and finally calcinations at 500 °C for 1 h. The Ru content of all catalysts were 5 mass % and the loading of

each catalyst was ~0.20 g per 2 g of alumina support. EDS analyses on Ru/Al_2O_3 catalysts revealed all constituent elements.

(2) $Ru/CeO_2/Al_2O_3$: A catalyst with irregular CeO_2 particles was first prepared on impregnating alumina support (Al_2O_3, 300 m^2/g, average diameter 1.2 mm) with a known amount of $Ce(NO_3)_3 \cdot 6H_2O$, followed by oven drying at 60 °C for 6 h and finally calcinations in air at 400 °C for 6 h. The resulting material was subsequently impregnated with an aqueous solution of $RuCl_3 \cdot 2H_2O$ (99.9%, STREM), followed by oven drying at 120 °C for 6 h and finally calcinations at 500 °C for 1 h under 0.2 SLPM H_2 flow. The Ru content of all catalysts were 5 mass % and the loading of each catalyst was ~0.20 g per 2 g of alumina support. EDS analyses on Ru/CeO_2 catalysts revealed all constituent elements.

(3) $Pt\text{-}Ru/CeO_2/Al_2O_3$: A catalyst with irregular CeO_2 particles was first prepared on impregnating alumina support (Al_2O_3, 300 m^2/g, average diameter 1.2 mm) with a known amount of $Ce(NO_3)_3 \bullet 6H_2O$, followed by oven drying at 60 °C for 6 h and finally calcinations in air at 400 °C for 6 h. The resulting material was subsequently impregnated with an aqueous solution of $PtCl_4$(99.9%, STREM) and $RuCl_3 \bullet 2H_2O$ (99.9%, STREM) with fixed Pt/Ru ratio, followed by oven drying at 90 °C for 6 h and finally reduced under flowing hydrogen at 600 °C for 1.5 h. For all of the supported Pt–Ru catalysts, the loading of Pt+Ru was adjusted to 5 and 10 wt. % and the molar ratio of Pt/Ru was varied to 0.5, 1.0 and 2.0,

respectively. The loading of each catalyst was ~0.20 g per 2 g of alumina support. EDS analyses on Pt-Ru/CeO_2 catalysts revealed all constituent elements.

(4) Rh/ $Ce_xZr_{1-x}O_2/Al_2O_3$: $Ce_xZr_{1-x}O_2$ nanocrystals of tube shape were synthesized under hydrothermal conditions. In general, $Ce(NO_3)_3 \bullet 6H_2O$ (99.9 %, Alfa Aesar) and $ZrO(NO_3)_2$ (STREM) with desired mole ratio was dissolved in deionized water to produce a transparent solution, to which was added NaOH (99 %, J. T. Baker) solution in a fixed amount with rigorous stirring for 10 min. The concentration of OH^- was controlled on adding deionized water. The solution contained some white colloid, which was transferred to a Teflon-lined stainless-steel autoclave. The optimum conditions for the preparation of a nanorod sample were $[OH^-]$ = 15 M, T = 150 °C, reaction duration 48 h, and then cooling to 23 °C. After that reaction, the solid products were filtered and rinsed with first deionized water and then ethanol. The major products from the hydrothermal synthesis were nanotubes of length 100-200 nm. The nanoparticles of all products have a characteristic light yellow color. The crystallinity, purity, crystal morphology and size of $Ce_xZr_{1-x}O_2$ products were analyzed with powder X-ray diffraction, transmission electron microscopy (TEM) and scanning electron microscopy (SEM) with energy-dispersive spectroscopy (EDS). All products were obtained as pure phases in a high yield.

(5) Rh/$Ce_xLa_{1-x}O_2$: Synthesis of $Ce_xLa_{1-x}O_2$ is similar to d). Precursors for this experiment include $Ce(NO_3)_3 \bullet 6H_2O$ (99.9 %, Alfa Aesar) and $La(NO_3)_3 \cdot 6H_2O$ (99.999 %, Alfa Aesar). The optimum conditions for the preparation of a nanorod sample were $[OH^-]$ = 15 M, T = 100 °C, reaction duration 10 h, and then cooling to 23 °C. After the metal oxide has been prepared, 5 wt% of Rh was deposited by impregnation method similar to b).

(6) Commercial three way catalysts were observed without further treatment.

(7) Catalysts with different ratio of Pt/Pd/Ru/Rh were prepared by the same procedures to prepare Pt-Ru bi metallic catalysts in c). CeO_2 loading different ratios of Pd/Pt/Rh were prepared by immersing methods in order to compare the selectivity of homemade catalyst with that of commercial catalysts. The weight percentage of CeO_2 was kept at 10 %wt. Precursors include $PtCl_2$, $PdCl_4$, and $RhCl_3$.

2. Characterization:

XRD data were collected on a powder diffractometer (Bruker D8, Cu Kα, 40kV/40mA). Semiquantitative microprobe analysis was performed with a scanning electron microscope (SEM, Hitachi S4700, Tokyo, Japan) equipped with an energy - dispersive spectroscopy (EDS) detector. Data were acquired with an accelerating voltage 15 kV. TEM images were obtained with a microscope (Philips TECNAI 20). Samples were generally prepared on depositing a drop of dilute nanoparticle solution in toluene onto carbon-coated Cu grids.

3. Apparatus and Product Analysis:

Tests of catalytic performance were performed with an apparatus shown in Figure 1. The system was equipped with mass-flow controllers and an HPLC pump (Jasco PU-2080 PLUS) for the carrier gas; the fed liquid contained an water/ethanol mixture of molar ratio 3 mol/mol (H_2O/C_2H_5OH). Reaction gases, supplied from high-pressure gas cylinders, had ultrahigh purity. Ethanol was analytic grade (Merck). The liquid was pumped to a steel chamber in which it was evaporated and in which it could be mixed (when desired) with an air stream from the mass-flow controllers. The gaseous mixture was fed to the reactor through silica tubing (inner diameter 4 mm, length ~15 cm). The temperature of the resulting gaseous mixture was maintained at 200 °C inside a furnace. The reactor was loaded with catalytic specimens of length up to 1.5 cm (~ 0.1g), and having a silica glass-wool seal between the catalyst and the reactor walls. Two thermocouples were placed inside the vaporizer and on top of the catalyst to monitor the temperature profiles. A six-port valve (Valco) served to direct samples of the effluent to the injection port of a GC–MS system (Trace Ultra DSQ) equipped with a PLOT capillary column (30 m×0.53 mm ID; Carboxen 1010, TCD detector, carrier gas=Ar, internal standard=N_2) to GC and a PLOT column (30 mm×ID 0.53 mm, Supel-Q, carrier gas=He) to a mass spectrometer. A condenser was placed before the latter column to condense and to remove H_2O, unreacted ethanol and other hydrocarbons from the gaseous stream.

The response factors of the TCD and MS detectors were determined by means of gaseous streams of known composition. The H_2 peak was integrated and compared against a calibration line produced from pure H_2 gas (>99.999% purity) before the experiments. The column oven was set at 45 °C and the TCD temperature was set at 200 °C. Argon or helium (>99.999% purity) served as carrier gas at a flow rate 72 ml/min with a split ratio 24. For the MS measurement, the mode of ionization was electron impact; data were collected in the full-scan mode. All experiments were performed at atmospheric pressure. In a typical experiment, after a fresh catalyst was placed in the reactor, the reactant stream with a water/ethanol molar ratio 3/1 was introduced into the reactor (T = 200 °C), in which it was heated, vaporized, and mixed with Ar carrier gas and air, and finally passed through the catalyst. The injection rate of ethanol was adjusted to control the C/O ratio. The temperature of the catalyst was increased rapidly to ~ 800 °C, and the product streams were fed into the GC-MS system. Freshly made catalysts were used to study the hydrogen selectivity at various C/O ratios. The overall reaction can be described as follows:

$$C_2H_5OH + 2H_2O + 1/2O_2 \rightarrow 2CO_2 + 5H_2$$

The catalytic activity was evaluated in terms of hydrogen selectivity (S_{H2}), which is defined as the molar ratio of the product H_2 (5mol expected from the above reactions per mol ethanol) to the hydrogen production per mole of ethanol (3 mol H_2/mol ethanol). Ethanol and other hydrocarbon products were condensed in water and analyzed with a mass spectrometer. In

all cases the results showed that most ethanol had reacted. For each catalyst, the reforming experiments were repeated several times and their results were reproducible.

4. Results:

(1) Ru/Al_2O_3 and $Ru/CeO_2/Al_2O_3$ catalyst[14]: Figure 2a shows the H_2 selectivity in different loading of Ru metal on Al_2O_3 support. The results indicate that the optimized condition for the maximum production of H_2 is from 5 wt% of Ru. Therefore, the following experiments were carried out under the same weight percentage of Ru metal for each catalyst. The effect of C/O ratio to hydrogen selectivity for Ru/Al_2O_3, $Ru/CeO_2/Al_2O_3$ and $Rh/CeO_2/Al_2O_3$ is shown in Figure 2b. The results indicate that the optimized condition for all catalysts is located at C/O = 0.7. The 5 wt %Ru/Al_2O_3 and $Ru/CeO_2/Al_2O_3$ catalyst show H_2 selectivity close to Rh/CeO_2 catalyst, which is a potential catalyst to replace Rh/CeO_2 catalyst due to lower price of Ru metal compare to Rh metal. The stability tests were performed with the optimized S_{H2} for the C/O ratio of each catalyst; S_{H2} is plotted as a function of duration on stream (Figure 3). For comparison purpose, Rh/CeO_2catalysts with CeO_2 nanorod, nanocube, and irregular particles were also presented. The results indicate that all catalysts suffered a small deactivation during 24 h on stream. For Rh-based catalysts, S_{H2} decreasing slightly from the initial value ~126 % to 100 % after 24 h on stream. On the other hand, S_{H2} of Ru-based catalysts also gradually

decreased from the initial value ~120 % to 90 % after 24 h on stream.

(2) $Rh/Ce_xZr_{1-x}O_2$: The catalyst with Zr doped oxide $Ce_xZr_{1-x}O_2$ with tube and particle shapes were test in varies C/O ratio. SEM images of $Ce_xZr_{1-x}O_2$ reveal tube and particle forms depending on the Ce/Zr ratio (Figure 4a). The H_2 selectivity study in varies C/O ratio is shown in Figure 4b. The results indicate that the best condition for H_2 production is at C/O = 0.7 for catalyst with x = 0.25 (S_{H2} ~ 120%).

(3) Pt_xRu_{1-x}/CeO_2: Synergistic interaction for the catalytic activity of ethanol reforming was investigated over various supported bimetallic Pt–Ru catalysts with CeO_2 nanoparticles. The Al_2O_3 was used as support materials by conventional impregnation method. The $Pt–Ru/CeO_2$ catalyst with Pt/Ru =0.5 exhibited highest activity and selectivity for H_2 (Figure 5). The H_2 selectivity for Pt-Ru bimetallic catalyst is less than $Ru/CeO_2/Al_2O_3$ catalyst, however, the bimetallic catalyst exhibit low preheating temperature of ~ 150 °C compare to Ru based catalyst of T ~ 300 °C.

(4) $Rh/Ce_xLa_{1-x}O_2$: Ternary oxide $Ce_xLa_{1-x}O_2$ with rod and irregular shape of nanocrystals were synthesized. The powder x-ray show fluorite type cubic structure and the SEM images show rod shape for x = 0.1 – 0.4 and irregular shape when $x \geq 0.5$(Figure 6). The catalyst of $5\%Rh/Ce_{0.9}La_{0.1}O_2$ (nanorod) shows hydrogen selectivity of 110±5%, but it suffered from the fluctuation problem of selectivity. Further studies of other Ce/La ratios are in progress.

(5) Three way catalysts: Several three ways catalysts were prepared to test their activity for ethanol reforming reaction, and they are summarized in Table 1. The results indicate that commercial 3-way catalysts exhibit low H_2 selectivity of ~ 35% and lab-made catalysts exhibit selectivity of H_2 larger than 60 %. The catalysts with Pd metal show lower S_{H2} than other catalyst without, which may be due to the deposition of carbon.

6. Conclusion:

The catalytic reforming of ethanol-water solution was investigated over noble metal/metal oxide nanoparticles (CeO_2, $Ce_xZr_{1-x}O_2$, and $Ce_xLa_{1-x}O_2$) using alumina as the supporting material. All catalysts could produce H_2 at selectivity from 70 to 120%. Catalytic activity of Ru/CeO_2 and $Rh/Ce_xZr_{1-x}O_2$ catalysts were comparable to the Rh/CeO_2 catalyst in producing H_2. Bimetallic Pt-Ru catalysts produced high selectivity to H_2 even at high C/O where initial heating decreases to ~150 °C. Commercial 3-way catalysts exhibit low H_2 selectivity, however, the as-prepared catalyst with varied compositions of Pt/Pd/Rh show selectivity of H_2 larger than 80 %. The effects of catalyst, flow rate, and C/O ratio on selectivities were examined. These results show that relative composition of noble metals play an important role and show very different selectivity in catalytic partial oxidation and preheating temperatures.

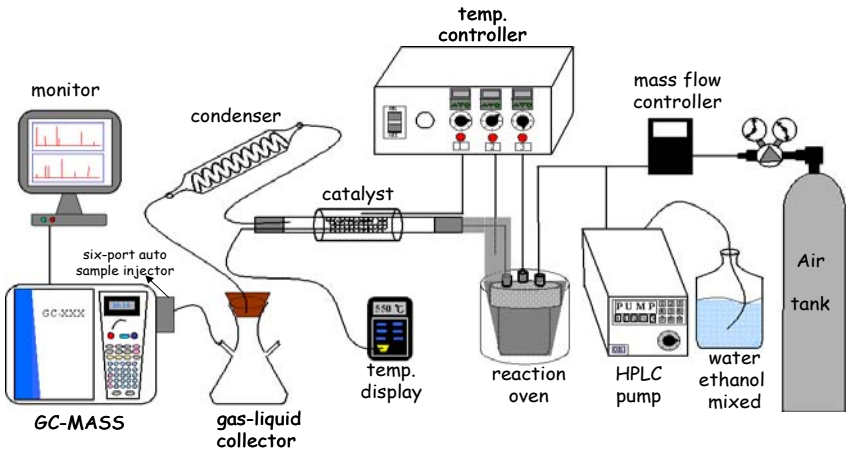

Figure 1. Schematic diagram of the experimental apparatus.

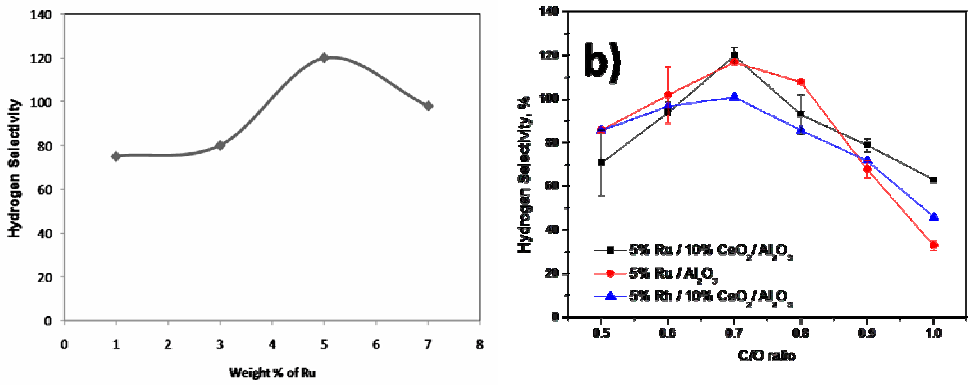

Figure 2. a) H_2 selectivity of catalysts with different loading of Ru metal. b) Hydrogen selectivity as a function of C/O ratio for Ru and Rh based catalyst.

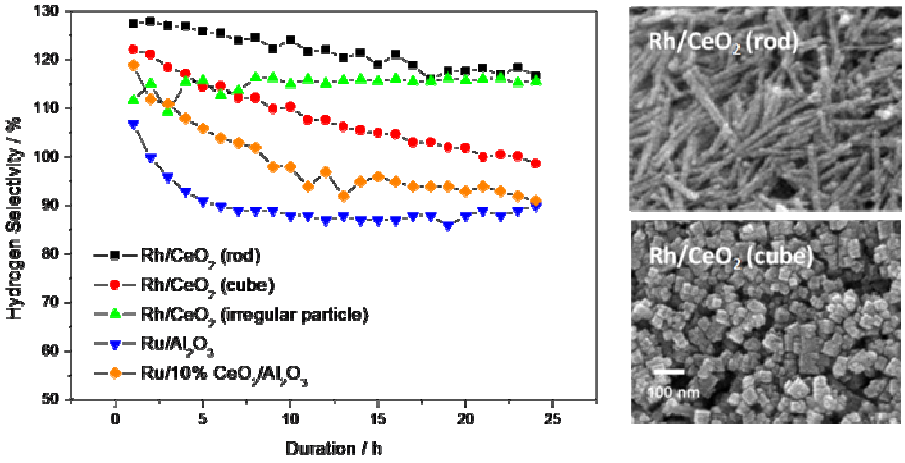

Figure 3. Hydrogen selectivity as a function of duration on stream.

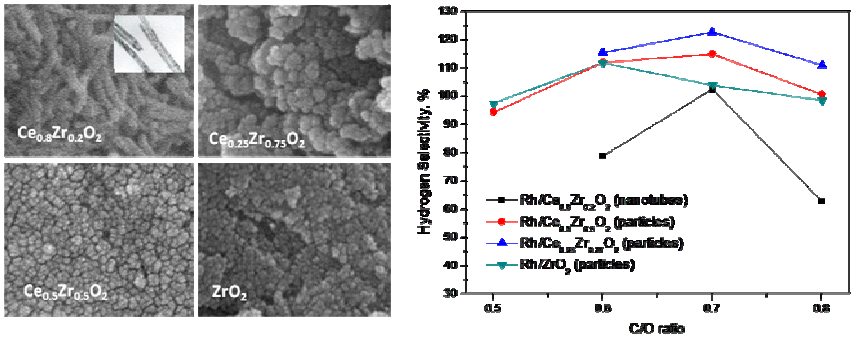

a) b)

Figure 4. a) SEM images of $Ce_xZr_{1-x}O_2$ nanomaterials. The inset is the corresponding TEM image for nanotube product. b) Hydrogen selectivity as a function of C/O ratio for $Rh/Ce_xZr_{1-x}O_2$ catalysts.

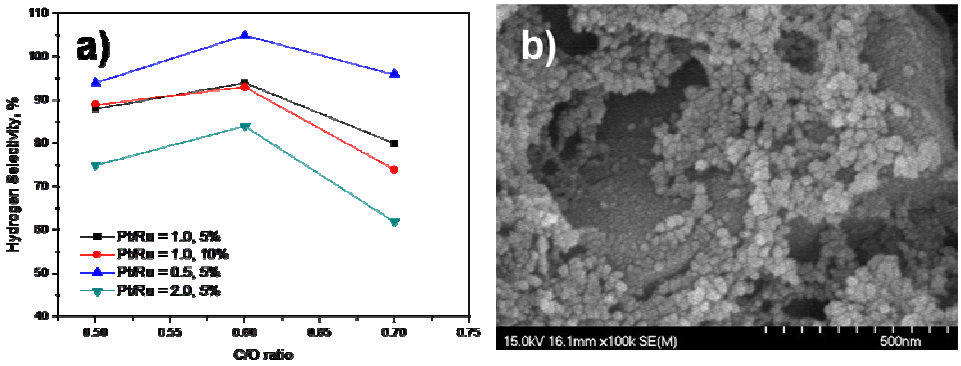

Figure 5. a) Hydrogen selectivity as a function of C/O ratio for catalysts with different Rt/Ru ratios. b) SEM image of Pt-Ru/CeO2 catalyst with Pt/Ru = 0.5.

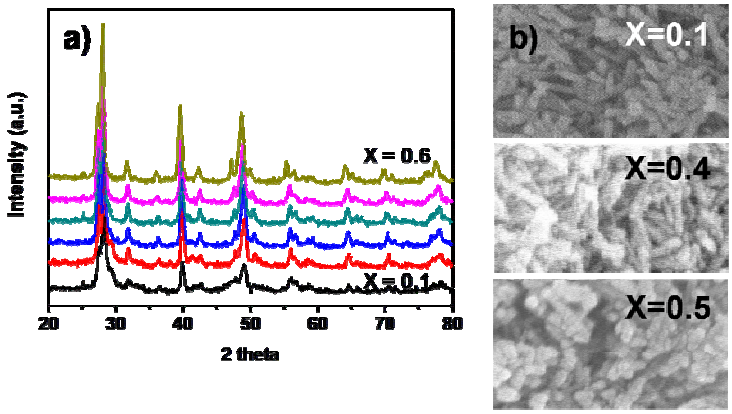

Figure 6: Powder X-ray patterns (x = 0.1 – 0.6) and SEM images of $Ce_xLa_{1-x}O_2$ (x = 0.1, 0.4 and 0.5).

Table 1: Summary of H_2 selectivity from commercial and lab-made catalysts.

No	*Description*	S_{H2}
	Commercial Catalyst	
1	Pt/Pd/Rh=5/0/1	40%
2	Pt/Pd/Rh=10/0/1	37%
3	Pt/Pd/Rh=5/5/1	30%
	As-synthesized (Pt/Pd/Rh=5/0/1)	
4	(5%Pt+1%Rh)/10%CeO_2/Al_2O_3	99%
5	(10%Pt+2%Rh)/10%CeO_2/Al_2O_3	96%
6	(15%Pt+3%Rh)/10%CeO_2/Al_2O_3	80%
	As-synthesized (Pt/Pd/Rh=10/0/1)	
7	(10%Pt+1%Rh)/10%CeO_2/Al_2O_3	88%
8	(20%Pt+2%Rh)/10%CeO_2/Al_2O_3	108%
9	(30%Pt+3%Rh)/10%CeO_2/Al_2O_3	111%
	As-synthesized (Pt/Pd/Rh=5/5/1)	
10	(5%Pt+5%Pd+1%Rh)/10%CeO_2/Al_2O_3	60%

References:

1. T.-E. Hsu, M.-C. Wu and C.-S. Lee, “Synthesis and steam reforming of ethanol over (CoxZn1-x)O catalysts” in Joint Symposium on Chemical Kinetics and Renewable Energy: from Gas phase to Condensed Phase, Hsinchu, 2007.
2. S.-F. Weng and C.-S. Lee, “Effect of Rhodium Nanoparticle Size to Ethanol Reforming Reaction” in Joint Symposium on Chemical Kinetics and Renewable Energy: from Gas phase to Condensed Phase, Hsinchu, Taiwan, 2007.
3. Y.-C. Chen, S.-F. Weng and C.-S. Lee, “Production of Hydrogen from Ethanol Reforming over Rh/CeO_2 - ZrO_2/Al_2O_3 Catalyst” in Joint Symposium on Chemical Kinetics and Renewable Energy: from Gas phase to

Condensed Phase, Hsinchu, Taiwan, 2007.

4. J.-F. Cheo, M. C. Lin and C.-S. Lee, “Ethanol to Hydrogen Conversion with Various Catalysts” in Joint Symposium on Chemical Kinetics and Renewable Energy: from Gas phase to Condensed Phase, Hsinchu, Taiwan, 2007.
5. G. A. Deluga, J. R. Salge, L. D. Schmidt and X. E. Verykios, Science, 2004**,** 303, 993-997.
6. W. I. Hsiao, Y. S. Lin, Y. C. Chen and C. S. Lee, Chem. Phys. Lett., 2007**,** 441, 294.
7. G. A. Camara, R. B. d. Lima and T. Iwasita, Electrochem. Comun., 2004**,** 6, 812.
8. H. A. Gasteiger, N. N. Ross and E. J. Cairns, J. Electrochem. Soc., 1994**,** 7, 1795.
9. H. X. Mai, L. D. Sun, Y. W. Zhang, R. Si, W. Feng, H. P. Zhang, H. C. Liu and C. H. Yan, J. Phys. Chem. B, 2005**,** 109, 24380-24385.
10. C. Tang, Y. Bando, B. Liu and D. Golberg, Adv. Mater., 2005, 17, 3005.
11. N. Laosiripojana and S. Assabumrungrat, Appl. Catal. A-Gen., 2005, 290, 200.
12. C. Diagne, H. Idriss and A. Kiennemann, Catal. Commun., 2002, 3, 565.
13. A. Haryanto, S. Fernando, N. Murali and S. Adhikari, Energy Fuels, 2005, 19, 2098.
14. J.-F. Cheo, M. C. Lin and C.-S. Lee, “Ethanol to Hydrogen Conversion with Ru/Al_2O_3 Catalyst”, Manuscript in preparation, 2007.

參、主要發現與結論

本計算團隊在乙醇轉氫、量子點-二氧化鈦太陽能系統及 SCC-DFTB 計算程式的研發等三大方向已經穩固地建立研發的能力，因為這些大化學系統的計算需要龐大的計算硬體及時間，SCC-DFTB 計算程式研發後，將減少計算時間，並供給反應速度常數作燃料電池的實際模擬，計算的結果也可與 VASP/CASTEP 固態系統的結果比較。

因為上述大系統計算需要很大的電腦系統，核能所在這方面如果能有效供應所需的 CPU's，則對這方面的發展，將有很大的幫助。

在實驗方面，交通大學已完整研發 Ru /CeO_2 /Al_2O_3 的催化系統，其效率優於 Schmidt 的 Rh /CeO_2 /Al_2O_3 系統，且便宜 25 倍。在計算方面，C_2H_5OH 在 Rh /CeO_2 上之分解機制已初步闡釋，至於 $(InN)_x$-OY(O)O-TiO_2 (x=0-10)的電子結構計算已能初步解釋 Y=B 及 P 的光電效率差異，並且提供$(InN)_x$-OY(O)O 之鍵能。

Resulting publications:

1. H. A. Witek, C. Koehler, T. Frauenheim, K. Morokuma and M. Elstner, "Relativistic parametrization of the self-consistent-charge density-functional tight-binding method. 1. Atomic wave functions and energies", J. Phys. Chem. A, 2007, 111, 5712-5719
2. H. A. Witek, G. Mazur, C. Koehler, T. Frauenheim, K. Morokuma and M. Elstner, "Relativistic parametrization of the

self-consistent-charge density-functional tight-binding method. 2. Molecular integrals", in preparation

3. G. S. Zheng, H. A. Witek, P. Bobadova-Parvanova, S. Irle, D. G. Musaev, R. Prabhakar and K. Morokuma, "Parameter calibration of transition-metal elements for the spin-polarized self-consistent-charge density-functional tight-binding (DFTB) method: Sc, Ti, Fe, Co, and Ni", J. Chem. Theory Comp., 2007, **3**, 1349
4. H. A. Witek, B. Trzaskowski, E. Malolepsza, K. Morokuma and L. Adamowicz, "Computational study of molecular properties of aggregates of C_{60} and (16,0) zigzag nanotube", Chem. Phys. Lett., 2007, 446, 87
5. E. Malolepsza, H. A. Witek and S. Irle, "Comparison of geometric, electronic, and vibrational properties for isomers of small fullerenes C_{20}–C_{36}", J. Phys. Chem. A**,** 2007, 111, 6649
6. Y.-R. Tzeng, P. Raghunath, S.-C. Chen and M. C. Lin, "A computational study of reaction pathways for the formation of indium nitride from trimethylindium with HN_3: Comparison of the reaction with NH_3 and that on TiO_2 rutile (110) surface", J. Phys. Chem. A, 2007, 111, 6781-88
7. H.-T. Chen, Y. M. Choi, M. Liu and M. C. Lin, "A Mechanistic Study on the Reduction of CeO_2 (111) and (110) by H_2", ChemPhysChem, 2007, 8, 849-55.
8. J.-G. Chang, J.-H. Wang and M. C. Lin, "A computational Study on the adsorption of BCl_x (x = 1-3) on TiO_2 anatase (101) and rutile (110) surfaces", J. Phys. Chem. A, 2007, 111, 6746-54.

9. H.-T. Chen, Y. M. Choi, M. Liu, and M. C. Lin, “A first-principles analysis for sulfur tolerance of CeO_2 in solid oxide fuel cells”, J. Phys. Chem. C, 2007, 111, 11117-11122.
10. P. Raghunath and M. C. Lin, “Computational study on the mechanisms and energetics of trimethylindium reactions with H_2O and H_2S”, J. Phys. Chem. A, 2007, 111, 6481-88.
11. Y. M. Choi, M. C. Lin and M. Liu, ”Computational Study of Catalytic Mechanism toward Oxygen Reduction on $La_{0.5}Sr_{0.5}MnO_3$ in Solid Oxide Fuel Cells”, 2007, Angew. Chem. Int. Ed., 46, 7214 .
12. Y. M. Choi, D. S. Mebane, M. C. Lin and M. Liu, “Oxygen Reduction on $LaMnO_3$-Based Cathode Materials in Solid Oxide Fuel Cells”, Chem. Mater, 2007, 19, 1690-1699.
13. J. J. Ho et al., “Density–Functional Calculation of the Adsorption and Reaction of CO and H_2O molecules over a $4Rh/CeO_2$ (111) Surface”, J. Phys. Chem. C, submitted.
14. W. I. Hsiao, Y. S. Lin, Y. C. Chen and C. S. Lee, “The Effect of the morphology of nanocrystalline CeO_2 on ethanol reforming”, Chem. Phys. Lett., 2007**,** 441, 294.
15. J.-F. Cheo, M. C. Lin and C.-S. Lee, “Ethanol to Hydrogen Conversion with Ru/Al_2O_3 Catalyst”, Manuscript in preparation, 2007.